

---

# Clustering of galaxies around AGN in the HSC

## Wide survey \*

**Yuji SHIRASAKI<sup>1,2</sup>, Masayuki AKIYAMA<sup>3</sup>, Tohru NAGAO<sup>4</sup>, Yoshiki TOBA<sup>5</sup>,  
Wanqiu HE<sup>3</sup>, Masatoshi OHISHI<sup>1,2</sup>, Yoshihiko MIZUMOTO<sup>1,2</sup>, Satoshi  
MIYAZAKI<sup>1,2</sup>, Atsushi J. NISHIZAWA<sup>6</sup> and Tomonori USUDA<sup>1,2</sup>**

<sup>1</sup>National Astronomical Observatory of Japan, 2-21-1 Osawa, Mitaka, Tokyo 181-8588, Japan

<sup>2</sup>Department of Astronomical Science, School of Physical Sciences, SOKENDAI (The Graduate University for Advanced Studies), 2-21-1 Osawa, Mitaka, Tokyo 181-8588, Japan

<sup>3</sup>Astronomical Institute, Tohoku University, 6-3 Aramaki, Aoba-ku Sendai, Miyagi 980-8578, Japan

<sup>4</sup>Research Center for Space and Cosmic Evolution, Ehime University, 10-13 Dogo-Himata, Matsuyama, Ehime 790-8577, Japan

<sup>5</sup>Academia Sinica Institute of Astronomy and Astrophysics, P.O. Box 23-141, Taipei 10617, Taiwan

<sup>6</sup>Institute for Advanced Research, Nagoya University, Furocho, Chikusa-ku, Nagoya 464-8602, Japan

\*E-mail: yuji.shirasaki@nao.ac.jp

Received ; Accepted

## Abstract

We have measured the clustering of galaxies around active galactic nuclei (AGN) for which single-epoch virial masses of the super-massive black hole (SMBH) are available to investigate the relation between the large scale environment of AGNs and the evolution of SMBHs. The AGN samples used in this work were derived from the Sloan Digital Sky Survey (SDSS) observations and the galaxy samples were from 250 deg<sup>2</sup> S15b data of the Hyper Suprime-Cam Subaru Strategic Program (HSC-SSP). The investigated redshift range is 0.6–3.0, and the masses of the SMBHs lie in the range  $10^{7.5}$ – $10^{10}$   $M_{\odot}$ . The absolute magnitude of the galaxy samples reaches to  $M_{320} \sim -18$  at rest frame wavelength 320 nm for the low-redshift

end of the samples. More than 70% of the galaxies in the analysis are blue. We found a significant dependence of the cross-correlation length on redshift, which primarily reflects the brightness dependence of the galaxy clustering. At the lowest redshifts the cross-correlation length increases from  $7 h^{-1}$  Mpc around  $M_{320} = -19$  mag to  $>10 h^{-1}$  Mpc beyond  $M_{320} = -20$  mag. No significant dependence of the cross-correlation length on BH mass was found for whole galaxy samples dominated by blue galaxies, while there was an indication of BH mass dependence in the cross-correlation with red galaxies. These results provides us a picture that the environment of AGNs studied in this paper is enriched with blue starforming galaxies, and a fraction of the galaxies are being evolved to red galaxies along with the evolution of SMBHs in that system.

**Key words:** galaxies: active — large-scale structure of universe — quasars: general

---

## 1 Introduction

Most of the galaxies have a supermassive black hole (SMBH) with mass grater than  $\sim 10^6 M_{\odot}$  at their center (Richstone et al. 1998). Observations of the local Universe have revealed that the mass of the SMBH correlates with the several properties of the bulge component of the host galaxy (Magorrian et al. 1998; Ferrarese & Merritt 2000; Gebhardt et al. 2000; Ho 2007). These observational evidences suggest that a SMBH and its host galaxy co-evolve in a coordinated way in spite of the nine orders of difference in their physical size scale (Kormendy & Ho 2013).

SMBHs grow through the accretion of gas from their host galaxies or large scale environment. Accretion in a secular mode, which arises through internal dynamical processes such as bar or disk instability or external processes driven by galaxy interaction, is one of the mechanism to deliver the gas into the SMBH (Kormendy & Kennicutt 2004). As the mass accretion rate of the secular mode cannot be as high as to maintain the activity seen in bright QSOs (Menci et al. 2014), this mode could operates in lower-luminosity AGNs.

A merger of galaxies can induce gravitational torques which drive inflows of cold gas toward the center of galaxies (e.g., Hopkins et al. 2008). Observational evidences have been obtained that show the relation between AGN activity and a galaxy merger (e.g., Sanders et al. 1988; Treister et al. 2012). The activity of the bright QSOs could be explained by this model. Although the accretion can

\* Based on data collected at Subaru Telescope, which is operated by the National Astronomical Observatory of Japan.

be the most efficient in this mode, it is also expected that AGN feedback promptly operates and stop the gas inflows when the mass of the SMBH becomes as higher as  $10^9 M_{\odot}$  (Fanidakis et al. 2013).

As an alternative process to make a SMBH evolve above  $10^9 M_{\odot}$ , quiescent gas accretion from the hot halo (Keres et al. 2009; Fanidakis et al. 2013) and/or recycled gas from evolving stars (Ciotti & Ostriker 2001, 2007) has been proposed. According to the predictions of semi-analytical modeling by Fanidakis et al. (2013), AGNs fueled in the hot-halo mode are located in more massive dark matter haloes than the AGNs fueled in the merger driven starburst mode.

The mass of the host dark matter halo that AGNs reside can be inferred from the auto-correlation function of AGNs at distance scale  $>1$  Mpc. According to the analysis of auto-correlation of SDSS QSOs by Ross et al. (2009), the halo mass is almost constant at  $\sim 2 \times 10^{12} h^{-1} M_{\odot}$  in the redshift range from 0.3 to 2.2. It is also possible to estimate the halo mass from the cross-correlation between AGNs and galaxies if the auto-correlation functions of galaxies are precisely obtained. According to the cross-correlation studies the dark matter halo mass estimated to be  $10^{12} - 10^{13.5} h^{-1} M_{\odot}$  depending on the detection wavelength of the AGNs (e.g. Hickox et al. 2009; Krumpe et al. 2012). Studies on clustering and/or environments of AGNs have also been reported elsewhere (e.g. Croom et al. 2005; Coil et al. 2009; Silverman et al. 2009; Donoso et al. 2010; Allevato et al. 2011; Bradshaw et al. 2011; Mountrichas et al. 2013; Zhang et al. 2013; Georgakakis et al. 2014; Krumpe et al. 2015; Ikeda et al. 2015; Krolewski & Eisenstein 2015)

In spite of a large number of AGN clustering studies published so far, the studies focused on the relation between the mass of the central SMBH, which is the most fundamental property on which the history of mass accretion is imprinted, and also the properties of galaxies such as color and luminosity function around it are very limited. Since the galaxy and its central SMBH is an open system in the large scale structure, it is inevitable, to a greater or lesser extent, to interact and coevolve with the surrounding galaxies. Thus the properties of the galaxies at the AGN environment can be the measures of the degree of progress on the galaxy formation and evolution in the dark matter halo where the AGN resides.

Shen et al. (2011) measured the clustering of QSOs for samples divided by their SMBH mass at redshifts 0.4–2.5 and didn't find significant dependence except for the most massive sample for which marginally larger clustering was found in  $\sim 2\sigma$  level. Komiya et al. (2013) examined dependence of the AGN-galaxy clustering on the SMBH mass at redshift range from 0.3 to 1.0 using the UKIDSS data for the galaxy samples, and found that the cross-correlation length increase above  $10^{8.2} M_{\odot}$ . Krumpe et al. (2015) measured clustering of soft X-ray and optically selected AGNs at redshifts from 0.16 to 0.36 and detected a weak dependence on the mass at significance level of  $2.7 \sigma$ , while they didn't detect significant dependence on the Eddington ratio. They conclude that the mass

dependence is the origin of the observed weak X-ray luminosity clustering dependence.

Extending the dataset of Komiya et al. (2013), Shirasaki et al. (2016) derived, for the first time as derived from statistically significant number of samples, color and absolute magnitude distributions of galaxies around the AGN, and found that the increase of the cross-correlation length found by Komiya et al. (2013) is due to the increase in the number density of red galaxies. Those results indicate that the most massive SMBHs are evolved in dark matter haloes more massive than the lower mass SMBHs, and the surrounding galaxies also evolve in a coordinated way with the SMBHs which are mostly located in the center of host halo. To extend further the study given in Shirasaki et al. (2016) up to redshifts  $\sim 3$ , which covers the era of the peak of star formation and mass accretion rate to SMBHs, we require a deeper wide multi-bands survey.

The Hyper Suprime-Cam Subaru Strategic Program (HSC-SSP) is a multi-band imaging survey conducted with the HSC on the 8.2m Subaru Telescope. The survey consists of three layers: Wide ( $1400 \text{ deg}^2$ ,  $r \sim 26$ ), Deep ( $27 \text{ deg}^2$ ,  $r \sim 27$ ), and UltraDeep ( $3.5 \text{ deg}^2$ ,  $r \sim 28$ ). The HSC-SSP Wide survey provides the first opportunity to investigate the environment of AGNs up to redshift three with unprecedented statistics. The purpose of this paper is, by utilizing the unique dataset of HSC-SSP Wide survey, to measure not only the clustering of galaxies around AGNs but also their color and luminosity distribution as a function of SMBH mass at five redshift groups from 0.6 to 3.0. The results obtained in this work would give us an unified picture of evolution of galaxies and SMBHs under the large scale structure of the Universe in their most important stage.

Throughout this paper, we assume a cosmology with  $\Omega_m = 0.3$ ,  $\Omega_\lambda = 0.7$ ,  $h = 0.7$  and  $\sigma_8 = 0.8$ . All magnitudes are given in the AB system. All the distances are measured in comoving coordinates. The correlation length is presented in unit of  $h^{-1} \text{Mpc}$ .

## 2 Datasets

### 2.1 AGNs

The AGN samples used in this paper were drawn from the QSO properties catalog of Shen et al. (2011) (S11) and SDSS DR12 Quasar catalog (DR12Q) of Paris et al. (2017). We used S11 catalog as a reference for the black hole (BH) mass estimate to be consistent with the previous works (Komiya et al. 2013; Shirasaki et al. 2016), and the BH masses derived from the DR12Q catalog and spectral measurements were calibrated with those derived in S11.

We divided the AGN samples according to their measured redshift and BH mass. The mass used in this analysis is based on the  $H\beta$ , Mg II, or C IV line width as given in the S11 and DR12Q catalogs. For AGNs drawn from the DR12Q catalog, the mass was calculated according to the formula

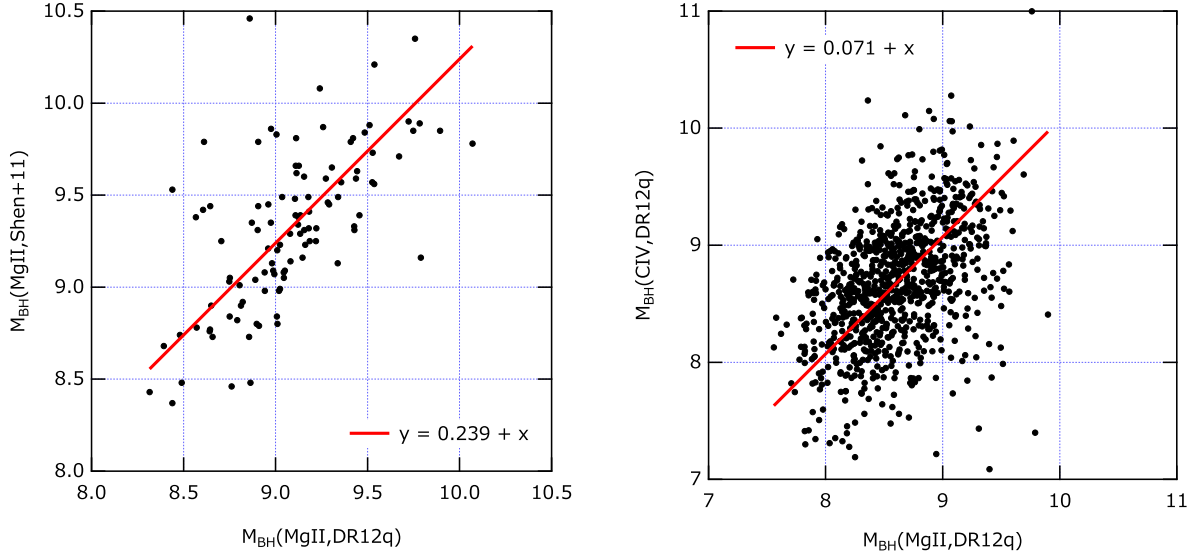


**Fig. 1.** Comparisons of BH masses derived by different methods for the same object. Left panel shows the comparison between the BH masses as given in S11 and those calculated for the same object in DR12Q using equation (1). Right panel shows the comparison between the BH masses calculated for an object in DR12Q using equation (1) and (2). The solid lines represent linear expressions fitted to the data points.

derived by Mejia-Restrepo et al. (2016) as follow:

$$M_{\text{BH,MgII}} = 8.05 \times 10^6 \left( \frac{L_{300}}{10^{44} \text{ erg s}^{-1}} \right)^{0.609} \left( \frac{\text{FWHM}(\text{Mg II})}{\text{km s}^{-1}} \right)^2, \quad (1)$$

$$M_{\text{BH,CIV}} = 5.71 \times 10^5 \left( \frac{L_{145}}{10^{44} \text{ erg s}^{-1}} \right)^{0.57} \left( \frac{\text{FWHM}(\text{C IV})}{\text{km s}^{-1}} \right)^2 \left( \frac{L_p(\text{C III])}}{L_p(\text{C IV})} \right)^{-2.09}, \quad (2)$$

where  $L_{300}$  and  $L_{145}$  are the continuum luminosity at 300 nm and 145 nm respectively,  $\text{FWHM}(\text{Mg II})$  and  $\text{FWHM}(\text{C IV})$  are the full width at half-maximum of the Mg II and C IV emission lines respectively, and  $L_p(\text{C III])}$  and  $L_p(\text{C IV})$  are peak luminosities of the corresponding lines. We measured the continuum luminosities,  $L_{300}$  and  $L_{145}$ , and the luminosity ratio,  $\frac{L_p(\text{C III])}}{L_p(\text{C IV})}$  directly from the SDSS spectra, while the FWHMs of the emission lines were taken from the DR12Q catalog.

To check the consistency between the BH masses derived by different relations, we compared them for the same objects. The left panel in Figure 1 shows the comparison of black hole masses given in S11,  $M_{\text{BH,MgII}}(\text{S11})$ , and those calculated for the same object in DR12Q,  $M_{\text{BH,MgII}}(\text{DR12Q})$ , using equation (1). We found there is a systematic offset of 0.24 dex and scatter of 0.22, so we have corrected for the offset to the mass calculated using equation (1).

The right panel in Figure 1 shows the comparison of black hole masses calculated for objects in DR12Q using equation (1),  $M_{\text{BH,MgII}}(\text{DR12Q})$ , and equation (2),  $M_{\text{BH,CIV}}(\text{DR12Q})$ . Systematic offset of 0.07 dex and scatter of 0.48 dex were found between them. Thus the offset

of  $M_{\text{BH,CIV}}(\text{DR12Q})$  to  $M_{\text{BH,MgII}}(\text{S11})$  was estimated to be 0.17, and the corresponding correction was made to  $M_{\text{BH,CIV}}(\text{DR12Q})$ . As mentioned in Mejia-Restrepo et al. (2016) and apparent from Figure 1,  $M_{\text{BH,CIV}}$  has a larger uncertainty than the mass measured based on other emission lines, so we used  $M_{\text{BH,MgII}}$ , whenever it was available, as a mass estimator in first priority. The AGN samples given the C IV BH mass are mostly at  $z \geq 2.3$ . The effect of the large uncertainty of the C IV BH mass is limited only to the results for  $z \geq 2.0$ .

Coatman et al. (2016) recently showed that an empirical correction to C IV BH masses based on the blueshift of C IV emission line reduces the uncertainty. To apply the correction an accurate measure of the AGN systemic redshift is required, thus we decided to use the relation of equation (2) which does not require precise spectroscopic measurements.

The systematic offset and scatter between  $M_{\text{BH,H}\beta}$  and  $M_{\text{BH,Mg II}}$  given in S11 catalog are 0.009 dex and 0.38 dex respectively as shown in Figure 10 of Shen et al. (2011), thus the correction to  $M_{\text{BH,H}\beta}$  is not required.

For AGNs appearing in both catalogs, we used the redshift and black hole mass of the S11 catalog. The redshift range of the AGNs was chosen to be 0.6–3.0, so that it overlaps with the highest redshift bin ( $z=0.6\text{--}1.0$ ) of the previous works (Komiya et al. 2013; Shirasaki et al. 2016) to cross check between both the results and extends up to the limit of sensitivity of this analysis. The BH mass range was set to  $10^7\text{--}10^{11}M_{\odot}$ . We selected 6166 AGNs which are in the redshift and BH mass range and are located within the footprint of HSC-SSP Wide survey.

## 2.2 Galaxies

The galaxy sample was collected from the Hyper Suprime-Cam Subaru Strategic Program (HSC-SSP) S15b Wide survey dataset. HSC-SSP is a three-layered, multi-band (*grizy* plus 4 narrow-band filters) imaging survey with the Hyper Suprime-Cam (HSC) (Miyazaki et al. 2012, 2017) on the 8.2m Subaru Telescope. The total area and the depth of observation will be  $1400 \text{ deg}^2$  with  $r \sim 26$  (Wide layer),  $27 \text{ deg}^2$  with  $r \sim 27$  (Deep layer), and  $3.5 \text{ deg}^2$  with  $r \sim 28$  (UltraDeep layer). The detail of survey itself is described in Aihara et al. (2017a), and the content of the S15b dataset is in Aihara et al. (2017b). The S15b dataset were analyzed through the HSC pipeline (version 4.0.1) developed by the HSC software team using codes from the Large Synoptic Survey Telescope (LSST) software pipeline (Ivezic et al. 2008; Axelrod et al. 2010). The photometric and astrometric calibrations are made based on data obtained from the Panoramic Survey Telescope and Rapid Response System (Pan-STARRS) 1 imaging survey (Magnier et al. 2013; Schlafly et al. 2012; Tonry et al. 2012).

The photometric magnitude used in this work is a CModel magnitude. The galactic reddening

was corrected according to the dust maps derived by Schlegel et al. (1998).

The analysis performed in this paper is based on two galaxy samples; one is the *i*-band detected sample which is drawn from all sources selected by the criteria for *i*-band as described below and measured to be brighter than 27 magnitude in *i*-band regardless of the detection in other four bands; the other is the four-bands detected sample which is selected by enforcing the same criteria for *griz*-bands except for the magnitude cut adapted only to *i*-band data, regardless of the detection in *y*-band. Since the observations in *y*-band are shallower than the others, the detection in *y*-band was not required to avoid the bias to redder galaxies. For the cross-correlation analysis, we used the *i*-band detected sample. When we measure the distribution of galaxy color and luminosity around AGNs, we used the four-bands detected sample. The term "detected" used here means that the source satisfies the criteria defined below and has a non-NULL magnitude.

The criteria used to select *i*-band detected samples are:

```
iflags_pixel_edge is not True
AND iflags_pixel_interpolated_any is not True
AND iflags_pixel_saturated_any is not True
AND iflags_pixel_cr_any is not True
AND iflags_pixel_bad is not True
AND icmodel_flux_flags is not True
AND icentroid_sdss_flags is not True
AND detect_is_tract_inner is True
AND detect_is_patch_inner is True
AND deblend_nchild = 0
```

where `iflags_pixel_edge` is true if the source is near the edge of the frame; `iflags_pixel_interpolated_any` is true if any pixels in the source footprint have been interpolated due to saturation or cosmic rays; `iflags_pixel_saturated_any` is true if any pixels are saturated; `iflags_pixel_cr_any` is true if any pixels are masked as cosmic rays; `iflags_pixel_bad` is true if any pixels are masked for non-functioning or in severely vignetted areas; `icmodel_flux_flags` is false if the `cmodel` measurement is failed; `icentroid_sdss_flags` is false if the SDSS centroiding algorithm is failed; `detect_is_tract_inner` and `detect_is_patch_inner` are true if the source is in the inner region of a tract and patch, which is used to select a source of primary detection; `deblend_nchild` is the number of children this source was deblended into. Similar flag checks were performed for the other bands.

In addition to the above criteria, we adapted a criterion:

```
flags_pixel_bright_object_center is not True
```

to remove the galaxy samples in bright source masks only for those which are located at  $\geq 2$  Mpc from the AGN. The bright source masks implemented in this data release are over-conservative in the choice of radius, so it has a drawback that decreases the significance of the clustering. Thus we did not adapt the bright source mask to the galaxy samples located at  $< 2$  Mpc from the AGN.

We found that there are non-negligible number of false detections in the deblended sources, especially at larger magnitudes. To remove the false detections, we selected only the deblended sources which are brighter than 27 mag in  $i$ -band and also brighter than  $m_{i,\text{top}} + 6$  mag, where  $m_{i,\text{top}}$  is an  $i$ -band magnitude brightest in the deblended sources which belong to the same parent.

### 2.3 AGN dataset selection

In the analysis of this paper, we treated each AGN and its surrounding galaxies as a set. We call hereafter the unit of the dataset as an AGN dataset. In this section we describe the criteria to include the AGN datasets for analysis.

For each AGN dataset, we measured the surface density of galaxies in annuli spaced by 0.2 Mpc out to 10 Mpc from the position of AGN. We kept only those AGN in which  $>60\%$  of the area of all annuli at  $\geq 2$  Mpc around it and  $>80\%$  of the area at  $< 2$  Mpc were included in the survey footprint and not masked by bright sources. By this selection, among the original 6166 AGN datasets, 346 datasets were removed for the  $i$ -band detected sample and 585 were removed for the four-bands detected sample. Thus 5820 and 5581 AGN datasets passed this selection for  $i$ -band and four-bands detected samples, respectively.

The spatial uniformity of the galaxy samples in the AGN field was also examined to identify the AGN dataset which are significantly contaminated by nearby galaxies and stellar groups or showing non-uniformity for any other reasons. For this purpose, we calculated two parameters for the radial number density distribution of galaxies,  $\chi^2$  and  $\sigma_{\text{max}}$ , where  $\chi^2$  is a square sum of the deviation from the number density distribution fitted to the observed data using equation (6), which will be derived in section 3.1,  $\sigma_{\text{max}}$  is a maximum deviation from the density distribution. Adapted criteria for those parameters are:  $\chi^2/n \leq 3.0$  and  $\sigma_{\text{max}} \leq 5$ . By this selection, 268 (236) AGN datasets were removed from the 5820 (5581) AGN datasets for the  $i$ -band (four-bands) detected sample. Thus 5552 (5345) AGN datasets passed all the above selections.

Figure 2 shows the mass vs redshift distribution of the AGNs which were selected according to the conditions described above and used in the cross-correlation analysis in this paper. Figure 3

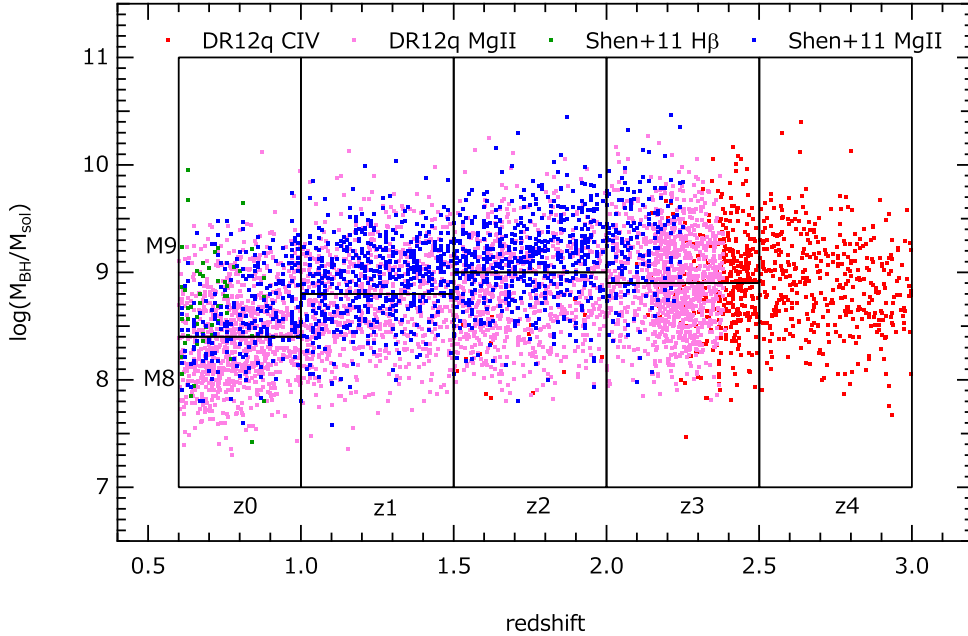


Fig. 2. Distribution of redshift and BH mass of 5552 AGNs which are used in cross-correlation analysis using *i*-band detected galaxy samples.

and 4 show histograms of redshift and black hole mass, respectively. We divided the redshift range into five groups as shown in Figure 2, which we call  $z_0$ ,  $z_1$ ,  $z_2$ ,  $z_3$  and  $z_4$  for  $z = 0.6\text{--}1.0$ ,  $1.0\text{--}1.5$ ,  $1.5\text{--}2.0$ ,  $2.0\text{--}2.5$ , and  $2.5\text{--}3.0$ , respectively. For each redshift group, except for  $z_4$ , the BH mass range was divided into two groups M8 and M9 so that each group has similar number of AGN rather than divided at the same mass. This is because the effect of sample variance becomes dominant when the number of AGN samples is small and it is difficult to homogenize the samples among different mass groups by the division at constant mass for all the redshifts. The mass group was divided at  $\log(M_{\text{BH}}/M_{\odot}) = 8.4, 8.8, 9.0$ , and  $8.9$  for  $z_0, z_1, z_2$  and  $z_4$  redshift groups, respectively, which allows us to make the statistical uncertainties even for both mass groups. The mass dependence for the  $z_4$  redshift group was not examined, since the number of samples in the  $z_4$  group is too small to do so.

Table 1 shows the number of AGN datasets which passed all the selection criteria described above for each dataset. The *i*-band detected galaxy samples were used for cross-correlation analysis, and the four-bands detected samples were used for deriving color distribution and luminosity function of clustering galaxies, and they were also used to measure the dependence of cross-correlation length on galaxy luminosity. The redshift matched samples were used for examining the BH mass dependence at each redshift.

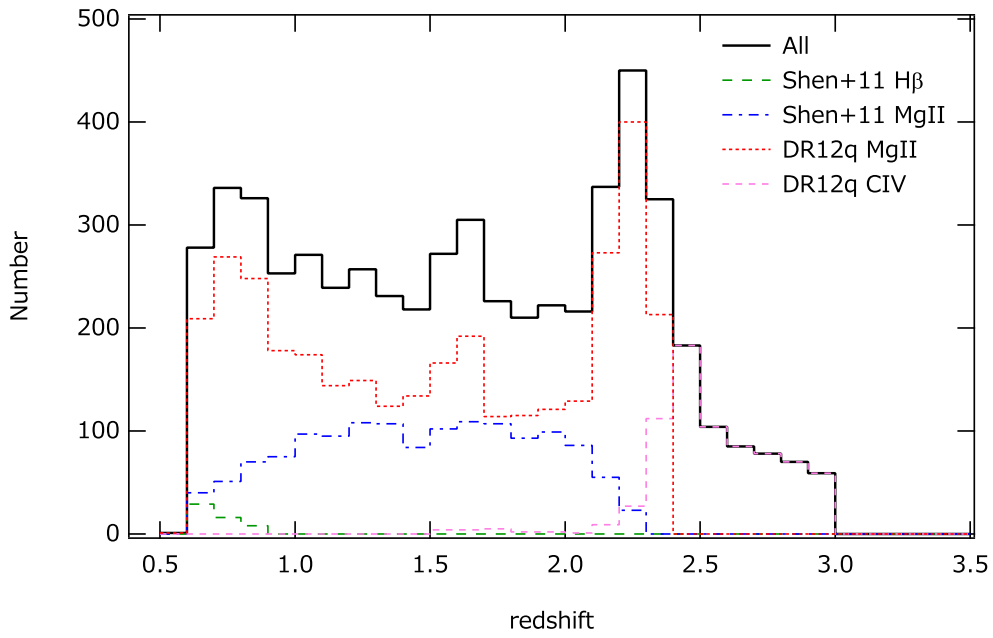


Fig. 3. Distribution of BH mass for the samples shown in Figure 2.

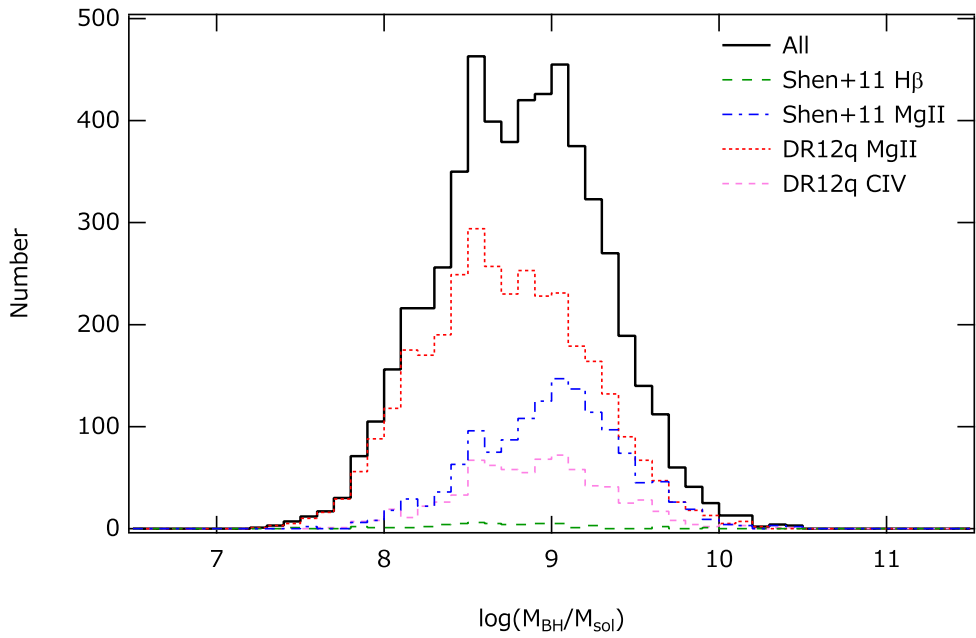


Fig. 4. Distribution of redshift for the samples shown in Figure 2.

**Table 1.** Number of AGN samples used in the analysis for each dataset.

| redshift group  | <i>i</i> -band detected |                        |     | four-bands detected |           |     |
|-----------------|-------------------------|------------------------|-----|---------------------|-----------|-----|
|                 | all                     | z-matched <sup>a</sup> |     | all                 | z-matched |     |
|                 | M8+M9                   | M8                     | M9  | M8+M9               | M8        | M9  |
| z0 <sup>b</sup> | 1194                    | 482                    | 482 | 1181                | 491       | 491 |
| z1 <sup>b</sup> | 1216                    | 506                    | 506 | 1212                | 500       | 500 |
| z2 <sup>b</sup> | 1235                    | 534                    | 534 | 1204                | 508       | 508 |
| z2 <sup>c</sup> |                         |                        |     | 1202                | 503       | 503 |
| z3 <sup>c</sup> | 1511                    | 640                    | 640 | 1385                | 581       | 581 |
| z4 <sup>c</sup> | 396                     |                        |     | 363                 |           |     |

<sup>a</sup> redshift matched samples. <sup>b</sup>  $M_{310}$  based samples for the four-bands detected samples. <sup>c</sup>  $M_{220}$  based samples for the four-bands detected samples.

### 3 Analysis method

#### 3.1 Cross-correlation length

The cross-correlation function between AGNs and galaxies was calculated using the method described in our previous papers (Shirasaki et al. 2011; Komiya et al. 2013; Shirasaki et al. 2016). The analysis method is briefly described here.

We assumed the power-law form of the cross-correlation function,

$$\xi(r) = \left(\frac{r}{r_0}\right)^{-\gamma}, \quad (3)$$

where  $r_0$  is a cross-correlation length and  $\gamma$  is a power-law index fixed to 1.8, which is a typical value found in previous studies on AGN-galaxy cross-correlation studies (e.g., Hickox et al. 2009; Coil et al. 2009; Krumpe et al. 2015). The projected cross-correlation function  $\omega(r_p)$  is expressed in an analytical form as:

$$\omega(r_p) = r_p \left(\frac{r_0}{r_p}\right)^\gamma \frac{\Gamma(\frac{1}{2})\Gamma(\frac{\gamma-1}{2})}{\Gamma(\frac{\gamma}{2})}, \quad (4)$$

where  $r_p$  is a projected distance from AGN and  $\Gamma$  is the Gamma function.  $\omega(r_p)$  is related to the observed average surface number density of galaxies  $n(r_p)$  as:

$$\omega(r_p) = \frac{n(r_p) - n_{\text{bg}}}{\bar{\rho}_0}, \quad (5)$$

where  $n_{\text{bg}}$  is an average surface number density of background galaxies integrated along the line of sight, and  $\bar{\rho}_0$  is an average of the number density of galaxies at AGN redshifts. From equations (4) and (5), the observed average surface number density of galaxies around AGNs can be expressed as:

$$n(r_p) = C(\gamma)\bar{\rho}_0 r_p \left(\frac{r_0}{r_p}\right)^\gamma + n_{\text{bg}}, \quad (6)$$

where  $C(\gamma) = \Gamma(\frac{1}{2})\Gamma(\frac{\gamma-1}{2})/\Gamma(\frac{\gamma}{2})$ . We fitted the model function of equation (6) to the surface number density derived by averaging over a group of AGN datasets, then obtained best fit parameters for the cross-correlation length  $r_0$  and the background density  $n_{\text{bg}}$ .

In calculating  $n(r_p)$ , we masked the central 10'' around each object to avoid blending problems with the AGN. Around a bright source there is a region where the number density of galaxy selected by the criteria described in section 2.2 is significantly reduced due to blending with the bright source and/or increase of the background noise level. That region needs to be counted as a dead region in calculating an effective area around AGN.

To estimate the dead region, we adapted a bright source flag to remove the galaxies near of bright sources, and the area of the masked region were calculated using the random catalog which was created avoiding the masked region with number density 100 arcmin<sup>-2</sup>. The random catalog we used is the one that is included in the S15b database. The bright source mask was applied only for those which are located  $\geq 2$  Mpc from the AGN as explained in section 2.2. To estimate the dead region at area of  $< 2$  Mpc, we calculated the correction factor from the average of the ratio of number density derived using masked ( $n_{\text{masked}}(r)$ ) and un-masked ( $n_{\text{unmasked}}(r)$ ) galaxy samples as following:

$$c(r) = \frac{n_{\text{unmasked}}(r)}{n_{\text{masked}}(r)} \quad (7)$$

$$n_{\text{corrected}}(r < 2\text{Mpc}) = \frac{n_{\text{unmasked}}(r < 2\text{Mpc})}{\langle c(r) \rangle_{r=2-10\text{Mpc}}} \quad (8)$$

To estimate  $\bar{\rho}_0$  in equation (6),  $\rho_0$  for each AGN dataset was estimated from the luminosity function which was derived by parametrizing the luminosity functions in literature. The luminosity function is expressed with the Schechter function:

$$\phi(M) = 0.4 \times \ln 10 \phi_* 10^{-0.4(M-M_*)(\alpha+1)} \exp\{-10^{-0.4(M-M_*)}\}. \quad (9)$$

The parameters  $\phi_*$ ,  $M_*$ , and  $\alpha$  were parametrized as a function of redshift  $z$  at rest-frame wavelengths 150 nm, 280 nm, SDSS  $u'$ ,  $g'$ , and  $r'$  band so that they approximated the parameters derived in literature (Gabasch et al. 2004, 2006; Dahlen et al. 2005, 2007; Parsa et al. 2016) for redshift  $z = 0.5-3.0$ . In total 40 sets of luminosity function parameters from those literature were used to determine the parametrization. Then they were interpolated as a function of wavelength.

The redshift parametrization was performed with the following functions:

$$\phi_* = \frac{\phi_{-18}}{0.4 \times \ln 10 \times 10^{0.4(18+M_*)(\alpha+1)} \exp\{-10^{0.4(18+M_*)}\}}, \quad (10)$$

$$\phi_{-18} = 10^{(a_0+a_1z)}, \quad (11)$$

$$M_* = b_0 + b_1z + b_2z^2, \quad (12)$$

**Table 2.** The coefficients of equations (11)–(13) used to calculate luminosity function in this analysis.

| parameter    | unit                             | wavelength band | coefficients                              |
|--------------|----------------------------------|-----------------|---|
| $\phi_{-18}$ | $\text{mag}^{-1}\text{Mpc}^{-3}$ | any             | $a_0 = -2.0, a_1 = -0.175$                |
| $M_*$        | mag                              | 150 nm          | $b_0 = -16.82, b_1 = -2.437, b_2 = 0.378$ |
| $M_*$        | mag                              | 280 nm          | $b_0 = -17.57, b_1 = -2.265, b_2 = 0.351$ |
| $M_*$        | mag                              | $u'$            | $b_0 = -18.40, b_1 = -1.932, b_2 = 0.294$ |
| $M_*$        | mag                              | $g'$            | $b_0 = -20.38, b_1 = -1.470, b_2 = 0.250$ |
| $M_*$        | mag                              | $r'$            | $b_0 = -21.60, b_1 = -0.936, b_2 = 0.157$ |
| $\alpha$     |                                  | any             | $c_0 = -1.2, c_1 = 0.0$                   |

$$\alpha = c_0 + c_1 z, \quad (13)$$

where  $\phi_{-18}$  represents luminosity density at  $M = -18$ . We used  $\phi_{-18}$  for the parametrization instead of using  $\phi_*$ , because  $\phi_*$  correlates with  $M_*$  parameter and is strongly affected by the uncertainty of  $M_*$ .  $\phi_{-18}$ , on the other hand, correlates with  $M_*$  more weakly than  $\phi_*$ , and its dependence on redshift and wavelength is rather small. The coefficients of equations (11)–(13) used in this analysis are summarized in Table 2. The comparison of these parametrization with the parameters in literature are shown in Figures 5–7.

The root mean square (RMS) of the difference between parameters from the literature and those calculated by parametrization of equations (10)–(13) are: 0.15, 0.28 mag, and 0.14 for  $\log(\phi_{-18})$ ,  $M_*$ , and  $\alpha$ , respectively. The error of  $\log \phi_{-18}$  by 0.15 corresponds to a systematic error of  $r_0$  by  $\sim 20\%$  for  $\gamma = 1.8$ .

The error of  $M_*$  significantly affects to the luminosity densities at bright end of  $M < M_*$ , as the slope of the luminosity function becomes steeper there. Thus comparison between the number densities at  $M < M_*$  calculated using the parameters from the literature  $\rho_{\text{lit}}$  and those calculated with the above parametrization  $\rho_{\text{par}}$  was made. According to the comparison, RMS of the relative error  $(\rho_{\text{lit}} - \rho_{\text{par}})/\rho_{\text{par}}$  is 0.36 for 40 sets of luminosity functions of the literature, which corresponds to an upper deviation of cross-correlation length of  $\delta r_0 = 0.28 \times r_0$ , that is 28% of the cross correlation length, and a lower deviation of  $\delta r_0 = 0.16 \times r_0$ , i.e. 16%, for  $\gamma = 1.8$ . When the comparison is made by extending to a lower luminosity side as  $M > -17$ , the RMS of the relative error is 0.16 for 20 sets of luminosity functions of  $z < 1.5$ , which corresponds to upper and lower deviation of 10% and 8% for  $r_0$ , respectively.

Then  $\rho_0$  is calculated as an integral of the product of the luminosity function and a detection efficiency  $\text{DE}(m)$  for apparent magnitude  $m$ . The detection efficiency was modeled with the following function:

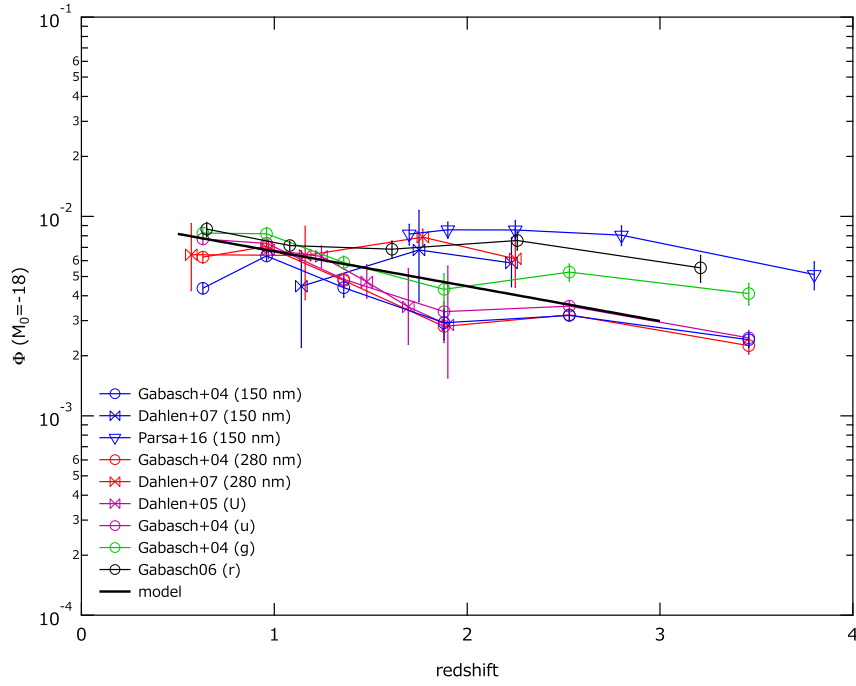


Fig. 5.  $\phi_{-18}$  parameters of equation (11) derived from literature (Gabasch et al. 2004, 2006; Dahlen et al. 2005, 2007; Parsa et al. 2016). Our parametrization is shown with a thick line.

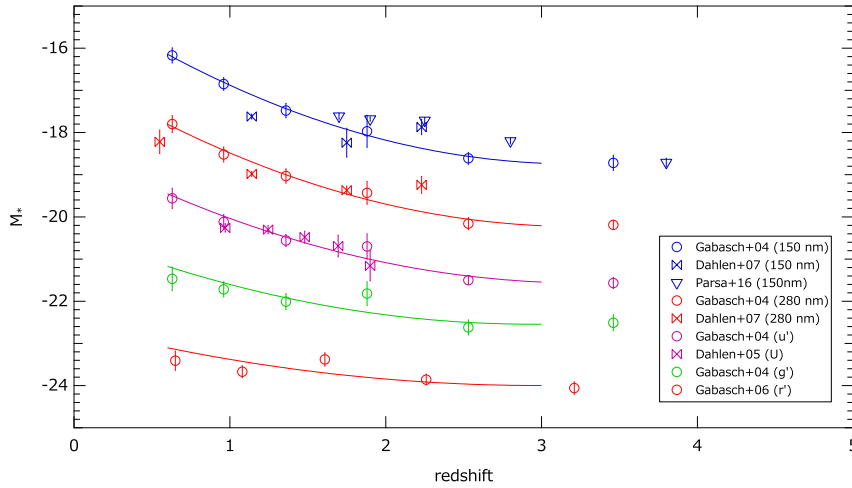
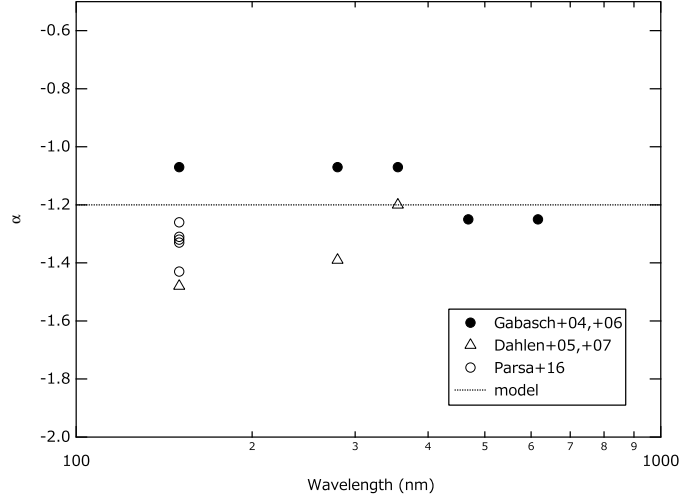


Fig. 6.  $M_*$  parameter of equation (12) derived from literature (Gabasch et al. 2004, 2006; Dahlen et al. 2005, 2007; Parsa et al. 2016). Our parametrization are shown with solid lines.



**Fig. 7.**  $\alpha$  parameter of equation (13) derived from literature (Gabasch et al. 2004, 2006; Dahlen et al. 2005, 2007; Parsa et al. 2016). Our parametrization is shown with a dotted lines.

$$DE(m) = \begin{cases} 1 & (m < m_{th}) \\ \exp(-(m - m_{th})^2/\sigma_m^2) & (m \geq m_{th}), \\ \exp(-(m - m_{th})^2/\sigma_m^2) \times \exp(-(m - m_{th2})^2/\sigma_{m2}^2) & (m \geq m_{th2} \geq m_{th}), \end{cases} \quad (14)$$

where  $m_{th}$  and  $m_{th2}$  represent the threshold magnitudes for a decrease in the detection efficiency,  $\sigma_m$  and  $\sigma_{m2}$  represent the attenuation widths. Two attenuation functions which have different threshold magnitudes and attenuation widths were required to fit the data accurately.

These parameters were obtained for each AGN dataset by fitting a model function to the observed magnitude distribution,  $N_{obs}(m)$  at  $m = 21-27$ . We assumed a power law form for the model function of the magnitude distribution which is expected for an ideal observation of 100% detection efficiency at any magnitude:

$$N_{org}(m) = c \times 10^{a(m-23)}, \quad (15)$$

Then the function  $N_{org}(m)DE(m)$  is fitted to the observed magnitude distribution  $N_{obs}(m)$ . The residuals between them are within the statistical error.

Using the  $DE(m)$  obtained from the fitting,  $\rho_0$  is calculated as:

$$\rho_0 = \int_{m_{low}-DM}^{m_{upp}-DM} \phi(M)DE(M+DM)dM, \quad (16)$$

where  $DM$  represents the distance modulus for the AGN redshift, and  $m_{low}$  and  $m_{upp}$  represent the magnitude range of the galaxy samples.

### 3.2 Color and absolute magnitude distributions for galaxies

The color ( $D_X$ ) and absolute magnitude ( $M_X$ ) distributions for galaxies around AGNs were derived by subtracting the distribution in an offset region ( $n_{\text{off}}$ ) from that at a central region of the AGN field ( $n_{\text{cen}}$ ) as followings (Shirasaki et al. 2016):

$$n(D_X) = n_{\text{cen}}(D_X) - n_{\text{off}}(D_X) \quad (17)$$

$$n(M_X) = n_{\text{cen}}(M_X) - n_{\text{off}}(M_X) \quad (18)$$

The offset region in this work is defined as an annular region at a projected distance from 7 to 9.8 Mpc from the AGN, and the central region is from 0.2 to 2 Mpc.

To calculate the color and absolute magnitude for the same rest frame bandpass at different redshifts, we performed SED fitting using the EAZY software developed by Brammer et al. (2008) and calculated color and magnitude at fixed bandpasses. For the redshift  $z_0$ ,  $z_1$ , and  $z_2$  groups ( $z = 0.6\text{--}2.0$ ), the color is defined as  $D_1 = M_{270} - M_{380}$  and the absolute magnitude is  $M_{310}$ , where  $M_{270}$ ,  $M_{380}$  and  $M_{310}$  represent absolute magnitudes at wavelengths 270, 380, and 310 nm, respectively. For the redshift  $z_2$ ,  $z_3$ , and  $z_4$  groups ( $z = 1.5\text{--}3.0$ ), the color is defined as  $D_2 = M_{165} - M_{270}$  and the absolute magnitude is  $M_{220}$ , where  $M_{165}$ ,  $M_{270}$ , and  $M_{220}$  represent absolute magnitudes at wavelengths 165, 270, and 210 nm, respectively. For redshift  $z_2$  group, we calculated the distributions for both definitions for comparison between them.

Although EAZY can be used to estimate photometric redshift, it was used here to interpolate the observed SEDs of all the sources assuming its redshift to be the same as the AGN redshift. This is because the photo- $z$  is not well constrained at redshifts explored in this work, as the structure around 400 nm, which is primarily used to determine the photo- $z$ , is out of the observed passband.

## 4 Results

### 4.1 Cross-correlation function

First we present the cross-correlation functions which were derived by using the  $i$ -band detected galaxy samples for each redshift group. To test also for the dependence on galaxy luminosity, two galaxy samples were constructed with different threshold magnitudes. The threshold magnitudes were chosen to be  $M_{90}$  and  $M_{50}$ , where  $M_{90}$  ( $M_{50}$ ) represents the absolute magnitude for which averaged detection efficiency estimated as described in section 3.1 is 90% (50%). The absolute magnitude is measured in  $i$ -band observer frame as calculated with  $m_i - DM$ , where  $m_i$  is  $i$ -band apparent magnitude and  $DM$  is distance modulus for AGN redshift. The values of  $M_{50}$  and  $M_{90}$  are summarized in the second and third columns of Table 3.

**Table 3.** Absolute magnitude threshold  $M_{50}$  and  $M_{90}$ .

| redshift | $m_i - DM$ |          | $M_{320}$ |          | $M_{220}$ |          |
|----------|------------|----------|-----------|----------|-----------|----------|
|          | $M_{50}$   | $M_{90}$ | $M_{50}$  | $M_{90}$ | $M_{50}$  | $M_{90}$ |
|          | mag        | mag      | mag       | mag      | mag       | mag      |
| z0       | -17.61     | -18.40   | -17.82    | -18.80   |           |          |
| z1       | -18.77     | -19.49   | -19.12    | -20.01   |           |          |
| z2       | -19.65     | -20.34   | -20.17    | -21.06   | -19.97    | -20.85   |
| z3       | -20.40     | -21.09   |           |          | -20.74    | -21.55   |
| z4       | -20.93     | -21.62   |           |          | -21.36    | -22.20   |

Figure 8 shows the distributions of average number density of galaxies with absolute magnitude brighter than  $M_{50}$  for five redshift groups. The model functions of equation (6) fitted to the observations are also plotted in the same figure. The corresponding cross-correlation functions calculated using equation (5) are shown in Figure 9. The estimated fitting parameters are summarized in upper parts of Table 4 for each threshold magnitude.

The statistical error of  $r_0$  was estimated by the jackknife method. Jackknife resamplings were made by omitting, in turn, each of the AGN datasets. Then  $r_0$  was calculated for each jackknife resampling and its error was estimated from their variance:

$$\sigma_{r_0}^2 = \frac{N-1}{N} \sum_{i=1}^N (r_{0,i} - \bar{r}_0)^2, \quad (19)$$

where  $r_{0,i}$  is a cross-correlation length obtained for the  $i$ -th jackknife sample,  $\bar{r}_0$  is the average of  $r_{0,i}$ , and  $N$  is the number of jackknife samples.

The cross-correlation lengths are plotted as a function of redshift in Figure 10 for each threshold sample. The result shows that the cross-correlation length increases as the redshift increases, and also is larger for more luminous galaxy samples. It is, therefore, important for examining the BH mass dependence after matching the distribution of redshift and galaxy luminosity for different BH mass groups.

To reduce the effect of redshift dependence in the comparisons between the different BH mass groups, we constructed redshift-matched samples for each redshift group. The redshift-matched samples were constructed by selecting the same number of AGN dataset for each  $\Delta z = 0.02$  bin.

The projected cross-correlation functions calculated for the redshift matched samples are shown in Figure 11 for four redshift groups z0, z1, z2 and z3. The mass dependence for z4 group was not examined due to poor statistic. In this figure, the circles represent lower BH mass groups (M8) and the squares represent higher BH mass groups (M9). The galaxy samples brighter than  $M_{90}$  were used. The estimated fitting parameters are summarized in the bottom part of Table 4.

The cross-correlation lengths are plotted as a function of BH mass in Figure 12. From these results, no significant difference between the two mass groups is seen.

For comparison with the previous results (Shirasaki et al. 2016), which was derived by using UKIDSS and SDSS data for galaxy samples, the result obtained for red galaxy samples ( $D_1 \geq 1.4$ ) as described in the next subsection are also plotted. In the work of Shirasaki et al. (2016), they calculated cross-correlation functions between AGNs and galaxies, which were mostly red galaxies, at redshifts  $< 1.0$ , and obtained the result that the cross-correlation length depends on BH mass but does not depend on redshift. Our current result at higher redshifts indicates its strong dependence on redshift and not on BH mass. The different behavior partly comes from the difference in the properties of galaxy samples, that is, the galaxy samples in the previous work are dominated by red type galaxies and mostly dimmer than  $L_*$ , while those of the current work are dominated by blue type galaxies and mostly consist of galaxies brighter than  $L_*$  at higher redshifts. As shown in the following subsection the clustering of galaxies significantly increases above  $L_*$ , which introduces redshift dependence to the cross-correlation length.

#### 4.2 Galaxy luminosity dependence of cross-correlation length

As larger clustering was indicated for more luminous galaxies as shown in Figure 10, we calculated cross-correlation lengths for flux-limited samples derived from the four-bands detected samples to examine the dependence on the luminosity of galaxies more closely. To calculate the absolute magnitude for the same rest frame bandpass at different redshifts, we performed SED fitting using the EAZY software developed by Brammer et al. (2008) and calculated the magnitude at a fixed bandpass. The observed magnitudes at  $g$ ,  $r$ ,  $i$ ,  $z$ , and  $y$  bands are used in the SED fitting. The flux-limited galaxy samples were constructed based on absolute magnitude  $M_{320}$  for  $z0$ ,  $z1$  and  $z2$  and  $M_{220}$  for  $z2$ ,  $z3$  and  $z4$ , where  $M_{320}$  and  $M_{220}$  represents the absolute magnitude at wavelength 320 nm and 220 nm, respectively.

Figure 13 shows the cross-correlation length as a function of average absolute magnitude of the galaxy sample brighter than the threshold magnitude in  $M_{310}$  or  $M_{220}$ , and Figure 14 shows it as a function of difference from the characteristic magnitude  $M_{*,\text{param}}$  of the parametrized luminosity function derived in section 3.1. From these figures, it is apparent that the cross-correlation length rapidly increases at magnitudes brighter than  $M_{*,\text{param}}$ . From Figure 13 the cross-correlation length looks almost independent of redshift when compared at the same absolute magnitude. The asymptotic values of the cross-correlation length at lower luminosity side, however, look different among the redshift groups.

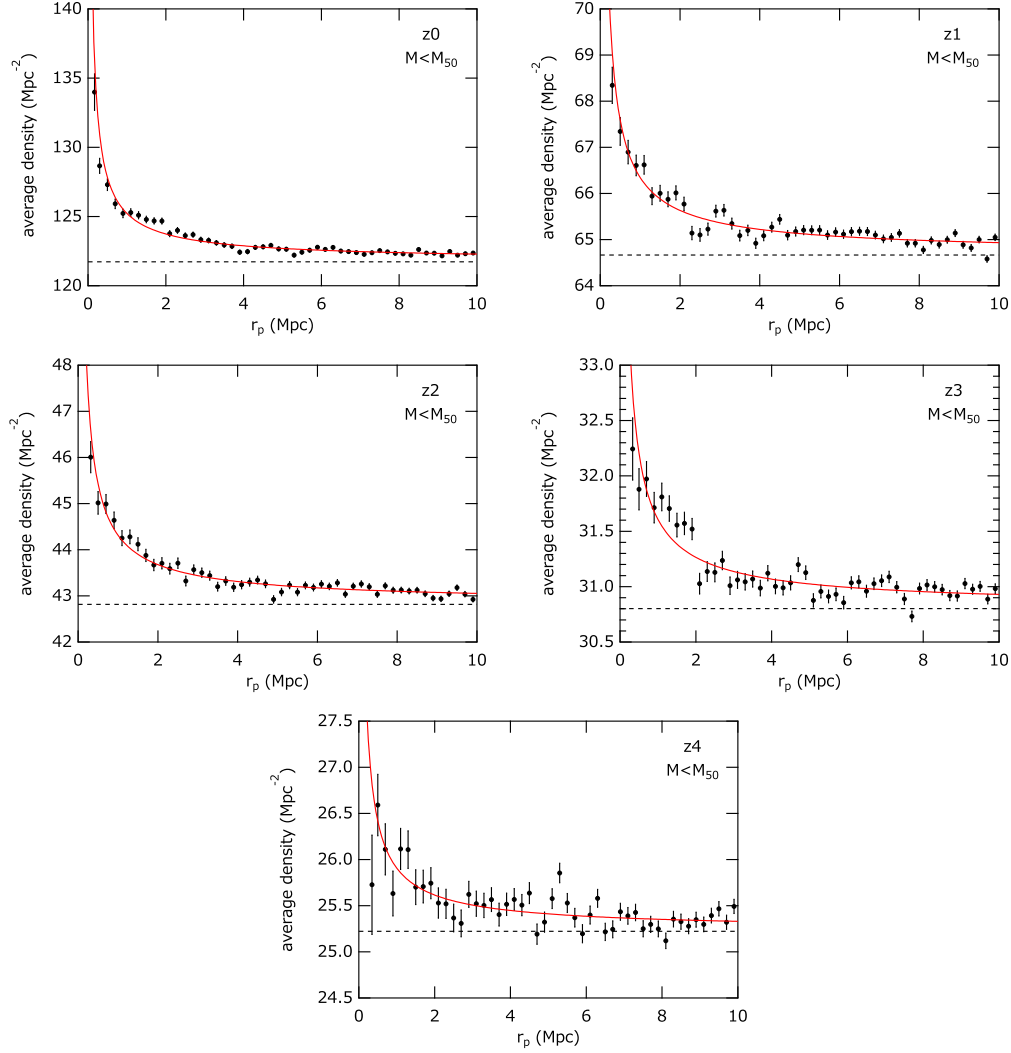


**Fig. 8.** Radial distribution of galaxy surface density around AGNs for each redshift group. *i*-band detected galaxy samples with absolute magnitude brighter than  $M_{50}$  are used, where  $M_{50}$  represents the magnitude where detection efficiency is 50%

To estimate the asymptotic value quantitatively, we fitted the following empirical formula to the observed data:

$$r_0 = r_{0,\min} + \exp\left(-\frac{M_X + 20}{\sigma_M}\right), \quad (20)$$

where  $r_{0,\min}$  represents an asymptotic cross-correlation length at low luminosities,  $M_X$  represents  $M_{310}$  or  $M_{220}$ , and  $\sigma_M$  corresponds to a slope of the curve at larger luminosities. The  $r_{0,\min}$  values obtained by the fitting are shown in Figure 15. Although they are the values obtained by the extrapolation from observed data points with an empirical formula, it may predict the cross-correlation length with low luminosity galaxies at higher redshifts. The result predicts that it increases as redshift increases and it reaches  $\sim 10 h^{-1}\text{Mpc}$  above  $z > 1.5$ , which indicates the redshift evolution of the auto-correlation length of AGNs and/or normal galaxies.

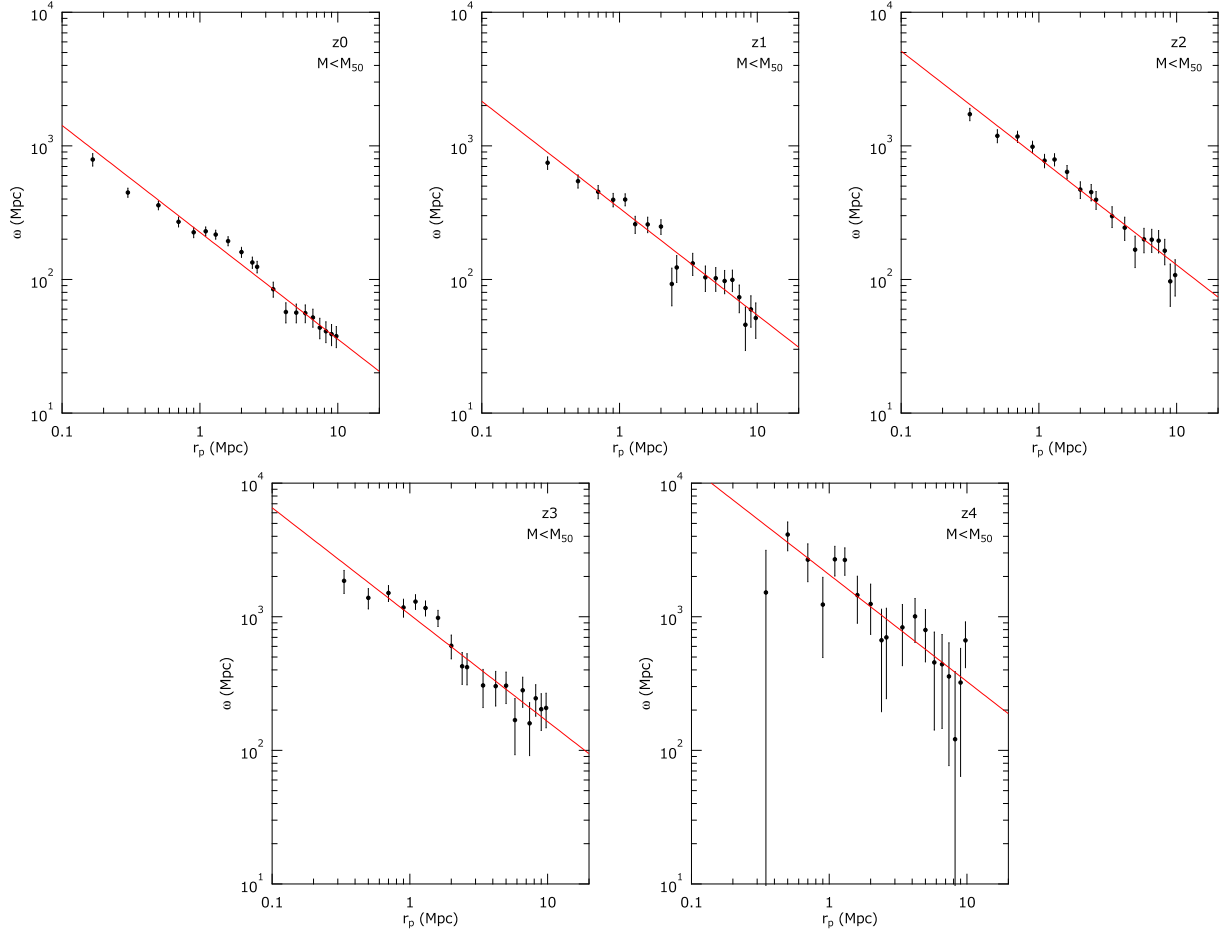
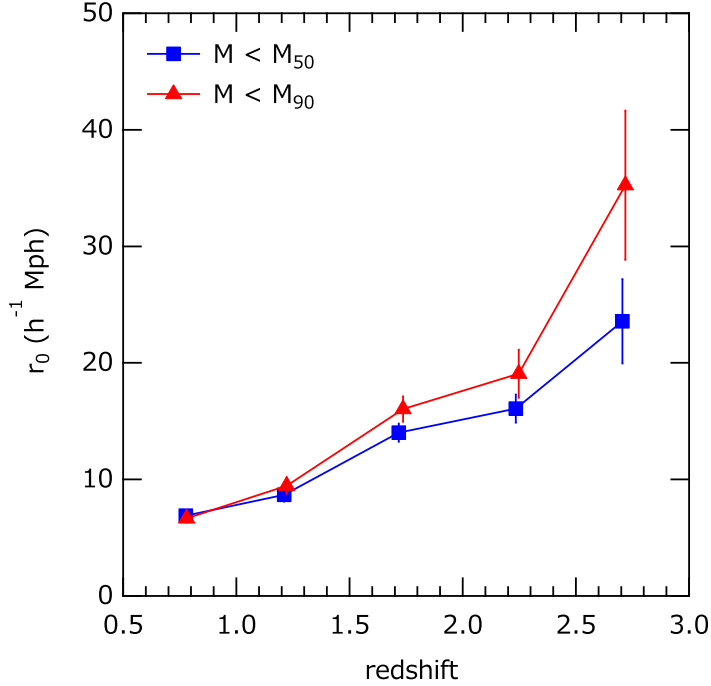


Fig. 9. Projected cross-correlation functions derived from data shown in Figure 8. Solid lines represents the power law model fitted to the data.

### 4.3 Color distributions of galaxies around AGNs

Color distributions of galaxies around AGNs were derived by the subtraction method described in section 3.2, and the results are shown in Figure 16 for color parameter  $D_1$  at  $z0$  to  $z2$  and in Figure 17 for  $D_2$  at  $z2$  to  $z4$ . Redshift matched AGN samples were used for this analysis. The galaxy samples used are the four-bands detected samples, and the threshold magnitude for the galaxy was chosen to be  $M_{50}$ , which is an absolute magnitude where average detection efficiency is 50%. The measured values of  $M_{50}$  are summarized in the fourth and sixth columns of Table 3.

The panels at the left end column in the figures show the excess color density of  $D_1$  or  $D_2$  distributions for combined M8+M9 groups, and they are placed in increasing order of their redshifts from top to bottom. The two panels at the right hand side of each row are those for M8 and M9 groups at the corresponding redshift, respectively. In the case of  $z4$  group, only the distribution of the whole mass group is shown, as the number of samples is too small to split the sample into two mass groups for the analysis of mass dependence.  $D_1$  is defined as a difference between magnitudes



**Fig. 10.** Cross-correlation length as a function of redshift. squares and triangles represent the cross-correlation length derived using galaxies brighter than  $M_{50}$  and  $M_{90}$  respectively, where  $M_{50}$  ( $M_{90}$ ) represents the magnitude where detection efficiency is 50% (90%).

at rest frame wavelengths of 270 nm and 380 nm for redshift  $z_0$ ,  $z_1$  and  $z_2$  groups, and  $D_2$  is a color between magnitudes at 165 nm and 270 nm for redshift groups of  $z_2$ ,  $z_3$  and  $z_4$ . The magnitudes were calculated by performing SED fitting using the EAZY software Brammer et al. (2008) as described in section 3.2.

The color distributions were fitted with a double Gaussian model in which the two Gaussian functions correspond to red (smaller  $D_1$ ) and blue (larger  $D_1$ ) galaxy types. The fitted model functions are plotted in the same figures. As can be seen from the figure, blue galaxies dominate the clustered component in our galaxy samples.

In the fit to the  $D_1$  distribution for  $z_2$ -(M8+M9) group shown in Figure 16, the Gaussian parameters for each components were not well constrained. This is partly because there is a tendency that the distribution of the blue component shifts to the redder side as the redshift increases, and the both components overlap each other in higher fraction for that group. Thus we fixed the Gaussian parameters of the red component to those obtained for  $z_1$ -(M8+M9) group. In the case of  $z_3$  and  $z_4$  shown in Figure 17, the red component is hardly seen, thus the Gaussian parameters for the red component were fixed to those obtained for  $D_2$  distribution of  $z_2$ -(M8+M9).

The fitting for the M8 and M9 samples were performed by fixing the Gaussian parameters to those obtained for the combined M8+M9 samples except for the  $z_0$  group. In the case of  $z_0$ ,

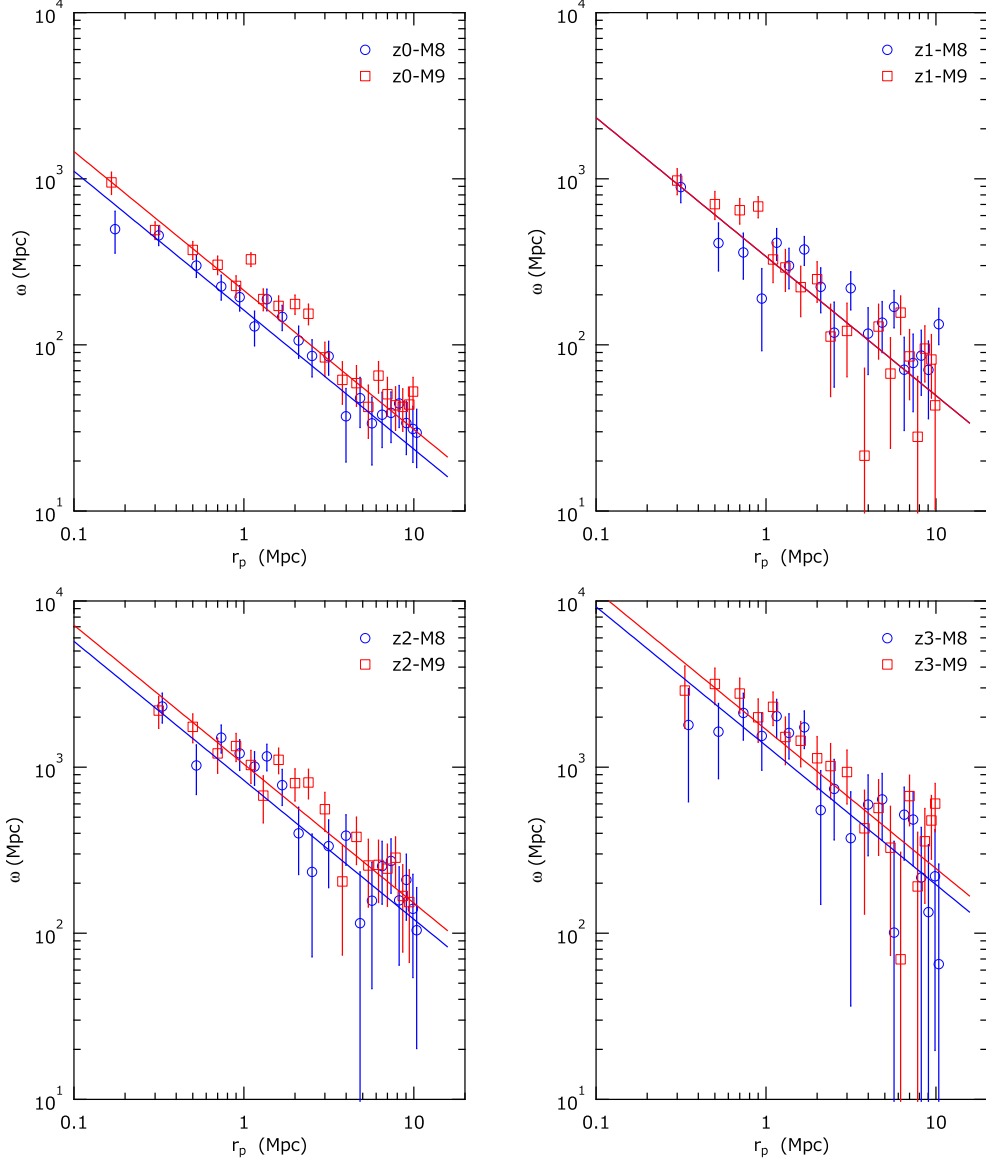


**Fig. 11.** Comparisons of projected cross-correlation functions derived for mass groups of M8 (circles) and M9 (squares). Each panel represents the result for redshift  $z_0$ ,  $z_1$ ,  $z_2$ , and  $z_3$ . Redshift matched AGN samples and galaxy samples brighter than  $M_{90}$  are used. Solid lines represent the power law model fitted to the data points.

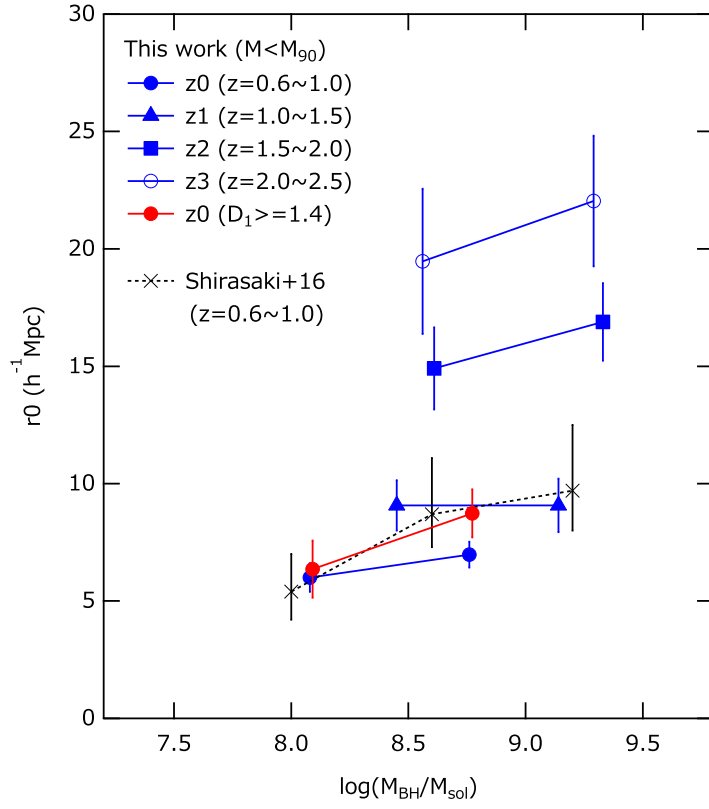


Fig. 12. Cross-correlation lengths plotted as a function average BH mass obtained for data shown in Figure 11.

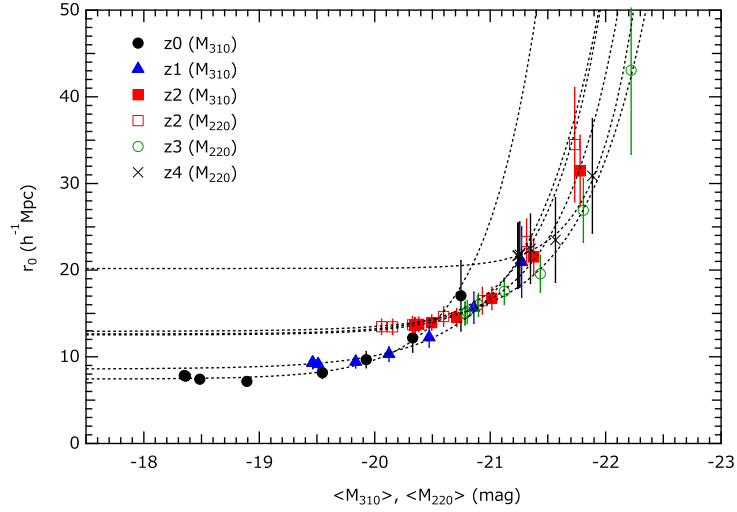


Fig. 13. Cross-correlation length as a function of absolute magnitude  $M_{310}$  or  $M_{220}$ . Dotted lines represent functions of equation (20) fitted to the data points.

**Table 4.** Fitting result of cross-correlation function.

| BH mass<br>$\log M_{\text{BH}}/M_{\odot}$                  | Redshift     | $n_{\text{AGN}}^{\text{a}}$ | $\langle \log M_{\text{BH}}/M_{\odot} \rangle^{\text{b}}$ | $\langle z \rangle^{\text{c}}$ | $r_0^{\text{d}}$<br>$h^{-1} \text{Mpc}$ | $\langle n_{\text{bg}} \rangle^{\text{e}}$<br>$\text{Mpc}^{-2}$ | $\langle \rho_0 \rangle^{\text{f}}$<br>$10^{-3} \text{Mpc}^{-3}$ |
|--|--------------|-----------------------------|---|--------------------------------|---|---|--|
| M < $M_{90}^{\text{g}}$ galaxy samples                     |              |                             |   |                                |   |   |  |
| 6.0–11.0 (M8+M9)   | 0.6–1.0 (z0) | 1194                        | 8.45  | 0.78                           | 6.66±0.36                               | 76.29±0.03  | 11.2   |
| 6.0–11.0 (M8+M9)   | 1.0–1.5 (z1) | 1216                        | 8.80  | 1.22                           | 9.46±0.69                               | 42.53±0.02  | 2.85   |
| 6.0–11.0 (M8+M9)   | 1.5–2.0 (z2) | 1235                        | 8.94  | 1.74                           | 16.05±1.09                              | 28.73±0.02  | 0.886  |
| 6.0–11.0 (M8+M9)   | 2.0–2.5 (z3) | 1511                        | 8.96  | 2.25                           | 19.07±2.06                              | 20.67±0.01  | 0.299  |
| 6.0–11.0   | 2.5–3.0 (z4) | 396                         | 8.90  | 2.72                           | 35.24±6.41                              | 16.89±0.02  | 0.0968   |
| M < $M_{50}^{\text{h}}$ galaxy samples                     |              |                             |   |                                |   |   |  |
| 6.0–11.0 (M8+M9)   | 0.6–1.0 (z0) | 1194                        | 8.45  | 0.78                           | 6.89±0.36                               | 121.73±0.04   | 15.5   |
| 6.0–11.0 (M8+M9)   | 1.0–1.5 (z1) | 1216                        | 8.80  | 1.22                           | 8.67±0.58                               | 64.67±0.03  | 4.92   |
| 6.0–11.0 (M8+M9)   | 1.5–2.0 (z2) | 1235                        | 8.94  | 1.74                           | 14.02±0.77                              | 42.82±0.02  | 1.85   |
| 6.0–11.0 (M8+M9)   | 2.0–2.5 (z3) | 1511                        | 8.96  | 2.25                           | 16.08±1.21                              | 30.80±0.02  | 0.777  |
| 6.0–11.0   | 2.5–3.0 (z4) | 396                         | 8.90  | 2.72                           | 23.58±3.62                              | 25.22±0.03  | 0.332  |
| Redshift matched AGN samples & M < $M_{90}$ galaxy samples |              |                             |   |                                |   |   |  |
| 6.0– 8.4 (M8)  | 0.6–1.0 (z0) | 482                         | 8.08  | 0.77                           | 6.00±0.61                               | 75.42±0.04  | 11.4   |
| 8.4–11.0 (M9)  | 0.6–1.0 (z0) | 482                         | 8.76  | 0.77                           | 6.98±0.55                               | 76.44±0.04  | 11.4   |
| 6.0– 8.8 (M8)  | 1.0–1.5 (z1) | 506                         | 8.45  | 1.22                           | 9.07±1.08                               | 42.03±0.03  | 2.85   |
| 8.8–11.0 (M9)  | 1.0–1.5 (z1) | 506                         | 9.14  | 1.22                           | 9.07±1.14                               | 43.05±0.03  | 2.86   |
| 6.0– 9.0 (M8)  | 1.5–2.0 (z2) | 534                         | 8.61  | 1.74                           | 14.91±1.75                              | 28.67±0.03  | 0.890  |
| 9.0–11.0 (M9)  | 1.5–2.0 (z2) | 534                         | 9.33  | 1.74                           | 16.89±1.65                              | 28.95±0.03  | 0.887  |
| 6.0– 8.9 (M8)  | 2.0–2.5 (z3) | 640                         | 8.56  | 2.25                           | 19.47±3.10                              | 20.75±0.02  | 0.299  |
| 8.9–11.0 (M9)  | 2.0–2.5 (z3) | 640                         | 9.29  | 2.25                           | 22.04±2.78                              | 20.61±0.02  | 0.300  |

<sup>a</sup> number of AGN datasets, <sup>b</sup> average of logarithm of BH mass, <sup>c</sup> average redshift, <sup>d</sup> cross-correlation length and its error, <sup>e</sup> average of projected number density of background galaxies, <sup>f</sup> average of the averaged number density of galaxies at the AGN redshift, <sup>g</sup> threshold magnitude -18.30, -19.40, -20.30, -21.00, -21.50 for z0, z1, z2, z3 and z4, <sup>h</sup> threshold magnitude -17.50, -18.70, -19.70, -20.30, -20.85 for z0, z1, z2, z3 and z4,

the peak positions of blue component is slightly different between the M8 and M9 groups, thus the Gaussian parameters for the blue component were derived independently. Those fitting parameters are summarized in Table 5.

The fractions of the blue galaxy for the combined mass groups are around 0.7–1.0, and there is a marginal indication that the blue fraction increases at higher redshifts. It should be noted that the comparison between the different redshifts need to be made by taking care about the difference in the galaxy samples. The galaxy samples at higher redshift are biased to more luminous galaxies, and it is also expected that the fraction of red galaxy increase as the luminosity as observed in the color-magnitude diagrams of the local galaxies. Thus the observed redshift dependence of the blue fraction is biased to the red component at higher redshift, and it is expected that the increase of the

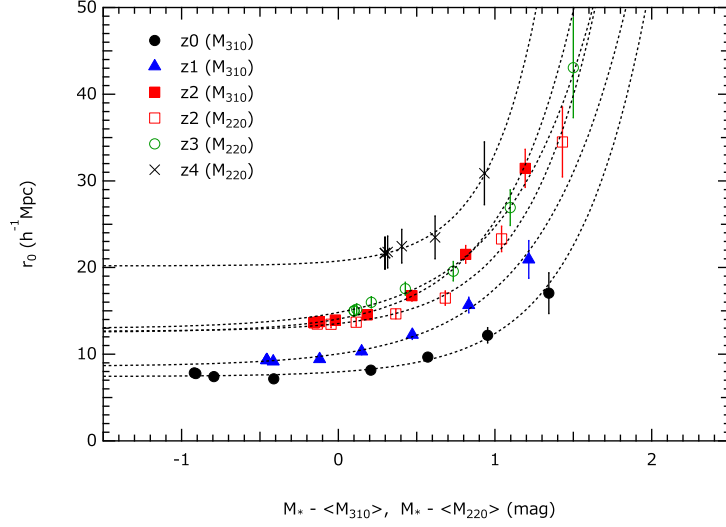


Fig. 14. Cross-correlation length as a function of  $M_* - M_{310,220}$ . Dotted lines represent functions of equation (20) fitted to the data points.

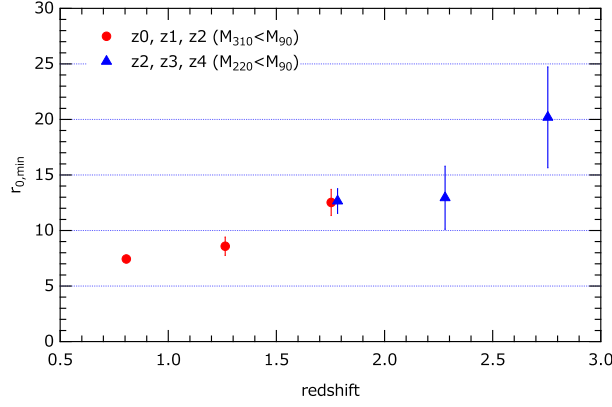


Fig. 15.  $r_{0,\min}$  parameter of equation (20) obtained by fitting to the data plotted in Figure 13

blue fraction is more or less enhanced if the bias is corrected.

As already mentioned above, it is found that the peak position of blue galaxy shift to redder side as redshift increases. We also found that the peak position is shifted to redder side for brighter galaxies of the same redshift, so the shift of the peak position to redder side at higher redshift is partly due the dependence of the color on the absolute magnitude of galaxy.

The obtained blue galaxy fractions are plotted in Figure 18 as a function of BH mass for each redshift group. A decreasing trend of blue fraction as BH mass is found for all redshifts except for z1. The result of z1 might be suffered from the sample variance, this can be tested by adding more samples from the upcoming HSC-SSP survey.

In the previous work of Shirasaki et al. (2016) that utilized SDSS and UKIDSS for galaxy samples, the fraction of blue galaxy was less than  $\sim 0.2$  at redshift group z0 of this work, as the

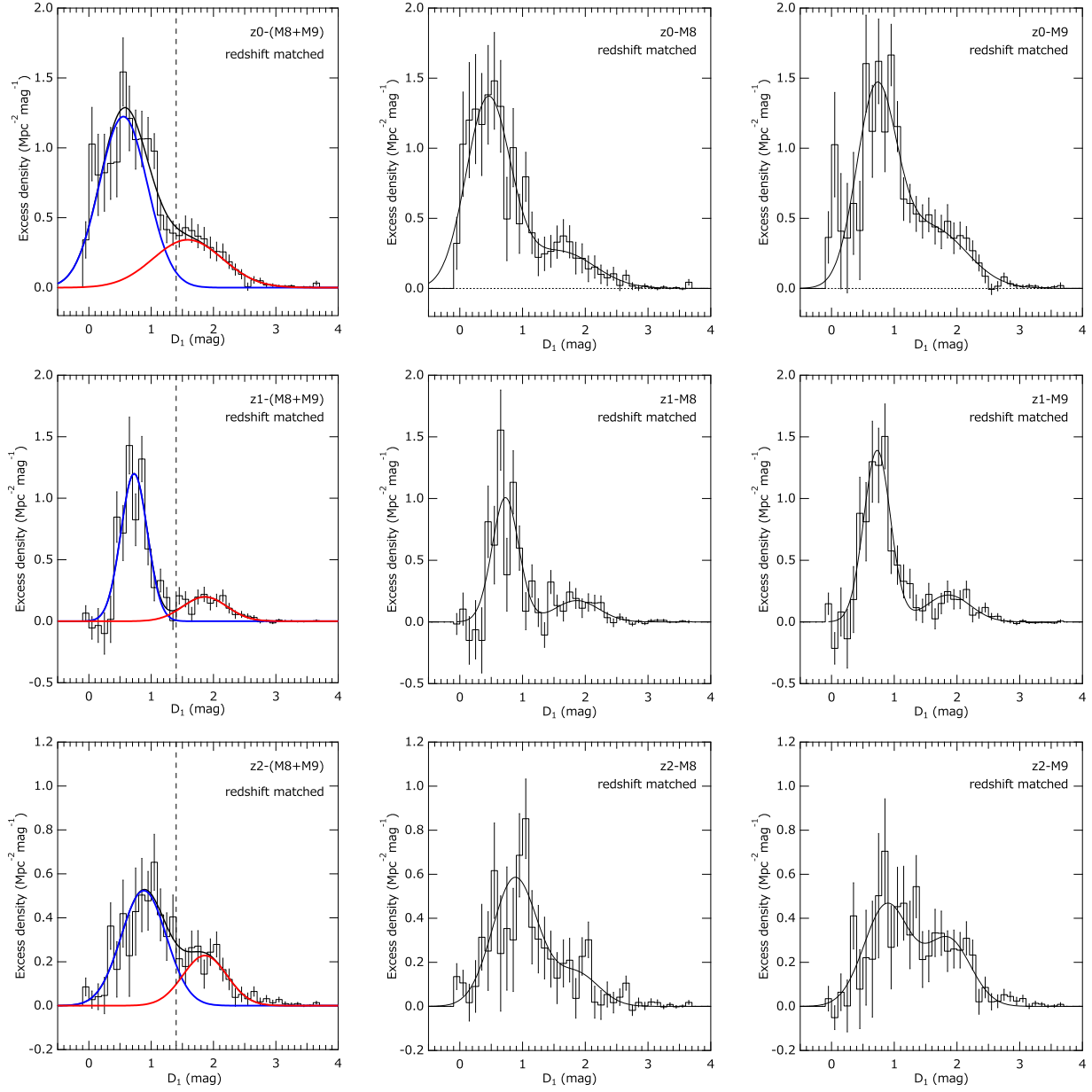


**Fig. 16.** Color ( $D_1$ ) distributions derived for redshift matched AGNs and  $< M_{50}$  galaxy samples. The panels on the left end column are the distributions for combined mass groups (M8+M9), and the two panels at the right hand side of each row are the distributions for individual mass groups of M8 and M9. Top three panels are those for redshift z0, and the middle and bottom panels are for z1 and z2, respectively. The solid lines represent the results of double Gaussian fitting. The dashed vertical lines represent the boundary defining blue and red galaxies in this paper.

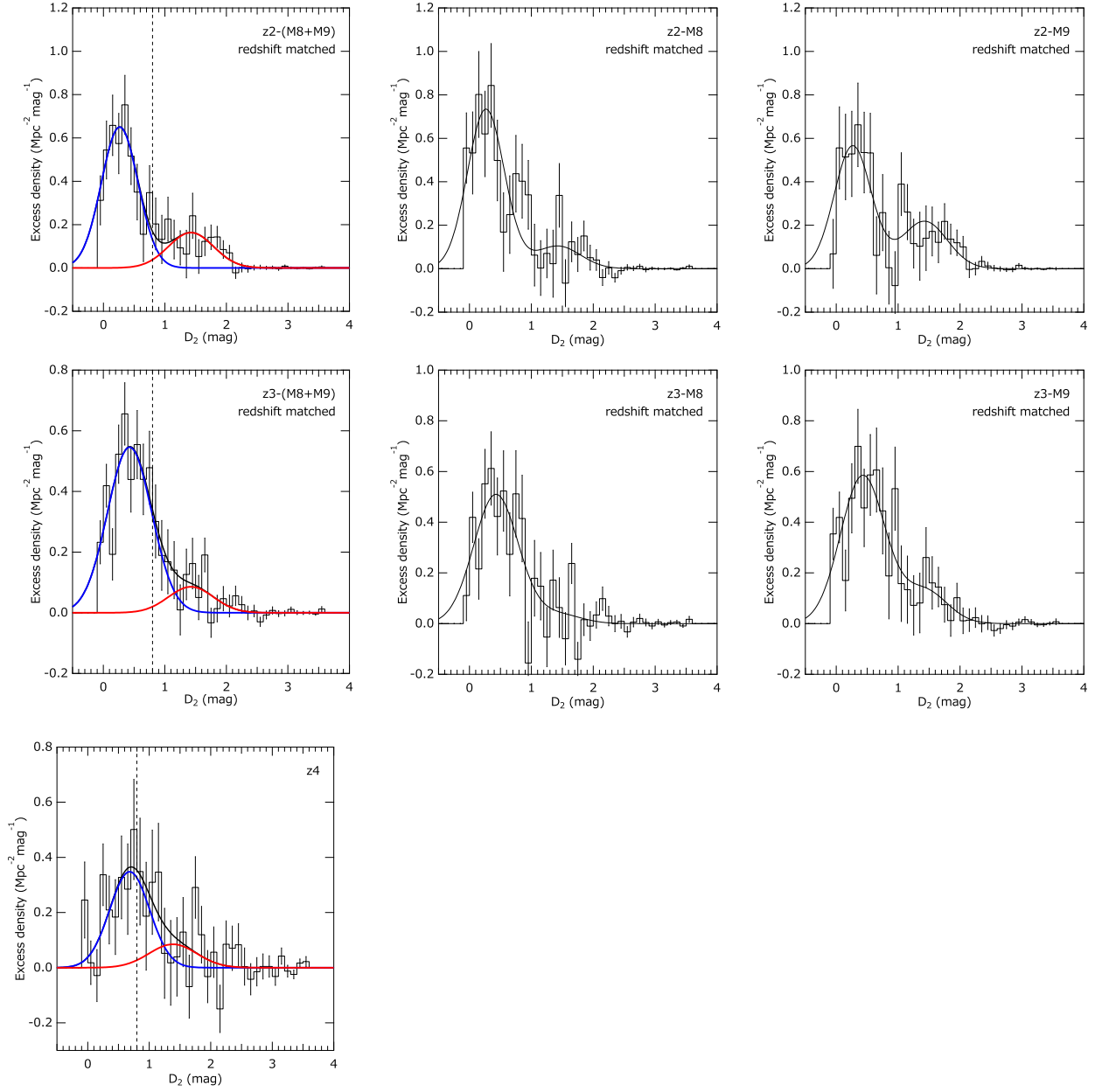


**Fig. 17.** Color ( $D_2$ ) distributions derived for redshift matched AGNs and  $< M_{50}$  galaxy samples. The panels on the left end column are the distributions for combined mass groups (M8+M9), and the two panels at the right hand side of each row are the distributions for individual mass groups of M8 and M9. Top three panels are those for redshift z2, and the middle and bottom panels are for z3 and z4, respectively. The solid lines represent the results of double Gaussian fitting. The dashed vertical lines represent the boundary defining blue and red galaxies in this paper.

**Table 5.** Fitting result for color distribution.

| redshift                      | BH mass<br>$\log M_{\text{BH}}/M_{\odot}$ | $n_{\text{AGN}}$ | $\mu_{\text{blue}}^{\text{a}}$ | $\sigma_{\text{blue}}^{\text{b}}$ | $\mu_{\text{red}}^{\text{c}}$ | $\sigma_{\text{red}}^{\text{d}}$ | $F_{\text{blue}}^{\text{e}}$ |
|-------------------------------|---|------------------|--------------------------------|-----------------------------------|-------------------------------|----------------------------------|------------------------------|
| $D_1$ : combined mass group   |   |                  |                                |                                   |                               |                                  |                              |
| 0.6–1.0 (z0)                  | 7.0–11.0 (M8+M9)                          | 982              | $0.55 \pm 0.05$                | $0.38 \pm 0.05$                   | $1.59 \pm 0.19$               | $0.56 \pm 0.08$                  | $0.71 \pm 0.09$              |
| 1.0–1.5 (z1)                  | 7.0–11.0 (M8+M9)                          | 1000             | $0.73 \pm 0.02$                | $0.21 \pm 0.02$                   | $1.86 \pm 0.06$               | $0.35 \pm 0.04$                  | $0.78 \pm 0.03$              |
| 1.5–2.0 (z2)                  | 7.0–11.0 (M8+M9)                          | 1016             | $0.88 \pm 0.04$                | $0.36 \pm 0.04$                   | 1.86                          | 0.35                             | $0.70 \pm 0.04$              |
| $D_2$ : combined mass group   |   |                  |                                |                                   |                               |                                  |                              |
| 1.5–2.0 (z2)                  | 7.0–11.0 (M8+M9)                          | 1006             | $0.27 \pm 0.04$                | $0.30 \pm 0.05$                   | $1.42 \pm 0.13$               | $0.37 \pm 0.08$                  | $0.76 \pm 0.06$              |
| 2.0–2.5 (z3)                  | 7.0–11.0 (M8+M9)                          | 1162             | $0.43 \pm 0.04$                | $0.36 \pm 0.04$                   | 1.42                          | 0.37                             | $0.86 \pm 0.05$              |
| 2.5–3.0 (z4)                  | 7.0–11.0                                  | 396              | $0.69 \pm 0.10$                | $0.33 \pm 0.09$                   | 1.42                          | 0.37                             | $0.79 \pm 0.17$              |
| $D_1$ : individual mass group |   |                  |                                |                                   |                               |                                  |                              |
| 0.6–1.0 (z0)                  | 7.0– 8.4 (M8)                             | 491              | $0.45 \pm 0.04$                | $0.35 \pm 0.04$                   | 1.59                          | 0.56                             | $0.76 \pm 0.03$              |
|                               | 8.4–11.0 (M9)                             | 491              | $0.71 \pm 0.04$                | $0.32 \pm 0.04$                   | 1.59                          | 0.56                             | $0.64 \pm 0.04$              |
| 1.0–1.5 (z1)                  | 7.0– 8.8 (M8)                             | 500              | 0.73                           | 0.21                              | 1.86                          | 0.35                             | $0.78 \pm 0.04$              |
|                               | 8.8–11.0 (M9)                             | 500              | 0.73                           | 0.21                              | 1.86                          | 0.35                             | $0.79 \pm 0.03$              |
| 1.5–2.0 (z2)                  | 7.0– 9.0 (M8)                             | 508              | 0.88                           | 0.36                              | 1.86                          | 0.35                             | $0.80 \pm 0.05$              |
|                               | 9.0–11.0 (M9)                             | 508              | 0.88                           | 0.36                              | 1.86                          | 0.35                             | $0.61 \pm 0.05$              |
| $D_2$ : individual mass group |   |                  |                                |                                   |                               |                                  |                              |
| 1.5–2.0 (z2)                  | 7.0– 9.0 (M8)                             | 503              | 0.27                           | 0.30                              | 1.42                          | 0.37                             | $0.85 \pm 0.05$              |
|                               | 9.0–11.0 (M9)                             | 503              | 0.27                           | 0.30                              | 1.42                          | 0.37                             | $0.68 \pm 0.05$              |
| 2.0–2.5 (z3)                  | 7.0– 8.9 (M8)                             | 581              | 0.43                           | 0.36                              | 1.42                          | 0.37                             | $0.93 \pm 0.07$              |
|                               | 8.9–11.0 (M9)                             | 581              | 0.43                           | 0.36                              | 1.42                          | 0.37                             | $0.81 \pm 0.05$              |

Redshift matched AGN datasets and four-bands (*griz*) detected galaxy brighter than  $M_{50}$  were used. <sup>a</sup>mean of the  $D_1$  or  $D_2$  distribution for blue component, <sup>b</sup>standard deviation of the  $D_1$  or  $D_2$  distribution for blue component, <sup>c</sup>mean of the  $D_1$  or  $D_2$  distribution for red component, <sup>d</sup>standard deviation of the  $D_1$  or  $D_2$  distribution for red component, <sup>e</sup>fraction of blue component.

galaxy sample was strongly biased to red type galaxy. In that work they also obtained the result that red galaxies of more luminous than  $M_{\text{IR}} = -20$  were strongly clustered around AGNs of  $M_{\text{BH}} > 10^{8.2} M_{\odot}$ . To test the consistency with the previous result on the cross-correlation with red galaxies, we calculated the cross-correlation lengths for red galaxies in the z0-M8 and z0-M9 groups separately.

We extracted red galaxies defined as  $D_1 \geq 1.4$ , and restricted their brightness to  $M_{310} < M_{90}$  ( $= -18.8$ ). To calculate the cross-correlation function, we should know the average number density of these galaxy types at the corresponding redshift,  $\bar{\rho}_{0,R}$ . It was estimated as  $\bar{\rho}_0(1 - f_{\text{blue}})$  using the blue fraction determined for z0-M8 group. Then we obtained the cross-correlation lengths for red galaxy samples as  $r_{0,\text{red}} = 6.35 \pm 1.22$  for z0-M8, and  $r_{0,\text{red}} = 8.73 \pm 1.02$  for z0-M9. The values of  $r_{0,\text{red}}$  are plotted in Figure 12 and compared with the previous work. They are consistent with each other.

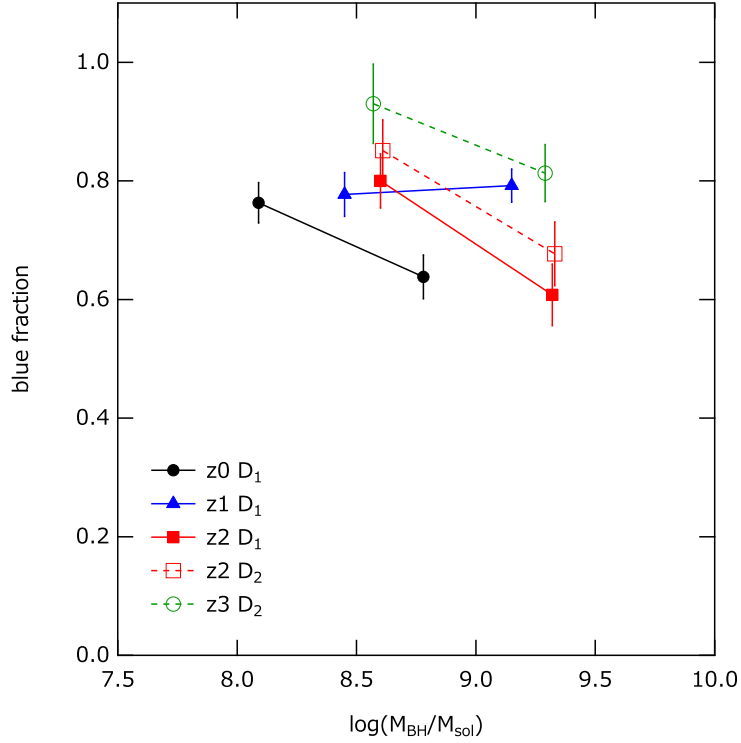


Fig. 18. Blue galaxy fraction as a function of BH mass. Galaxy samples brighter than  $M_{50}$  were used.

#### 4.4 Luminosity functions of galaxies around AGNs

Next we examined the absolute magnitude distributions of the galaxy clustered around AGNs. The left (right) panel of Figure 19 shows the distributions of  $M_{310}$  ( $M_{220}$ ) for z0, z1 and z2 (z2, z3 and z4) redshift groups. The excess densities were calculated as in equation (18) and corrected for their detection efficiencies calculated as described in section 3.1. They are plotted for  $M_{310/220} < M_{50}$ .

In the same figure magnitude distributions expected at each redshift are also plotted with solid lines. The expected values were calculated from the luminosity function at the corresponding redshifts by multiplying it by a factor derived from the cross-correlation length of each data sample ( $M_{50}$  galaxy sample). The multiplying factor was calculated as:

$$\frac{n_{\text{IN}} - n_{\text{OUT}}}{\rho_0} = \frac{2C(\gamma)r_0^\gamma}{3 - \gamma} \left( \frac{r_{\text{max,IN}}^{3-\gamma} - r_{\text{min,IN}}^{3-\gamma}}{r_{\text{max,IN}}^2 - r_{\text{min,IN}}^2} - \frac{r_{\text{max,OUT}}^{3-\gamma} - r_{\text{min,OUT}}^{3-\gamma}}{r_{\text{max,OUT}}^2 - r_{\text{min,OUT}}^2} \right), \quad (21)$$

where  $n_{\text{IN}}$  ( $n_{\text{OUT}}$ ) represents the surface number density at an inner (outer) region of the AGN field defined by annulus from  $r_{\text{min,IN}}$  to  $r_{\text{max,IN}}$  (from  $r_{\text{min,OUT}}$  to  $r_{\text{max,OUT}}$ ), and the right-hand side of the equation is calculated by integrating the equation (6). The boundary radii are  $r_{\text{min,IN}} = 0.2$ ,  $r_{\text{max,IN}} = 2.0$ ,  $r_{\text{min,OUT}} = 7.0$ , and  $r_{\text{max,OUT}} = 9.8$ . The arrows at the top of the figure indicate 90% detection limits. These results show overdensity against expectations from the luminosity function

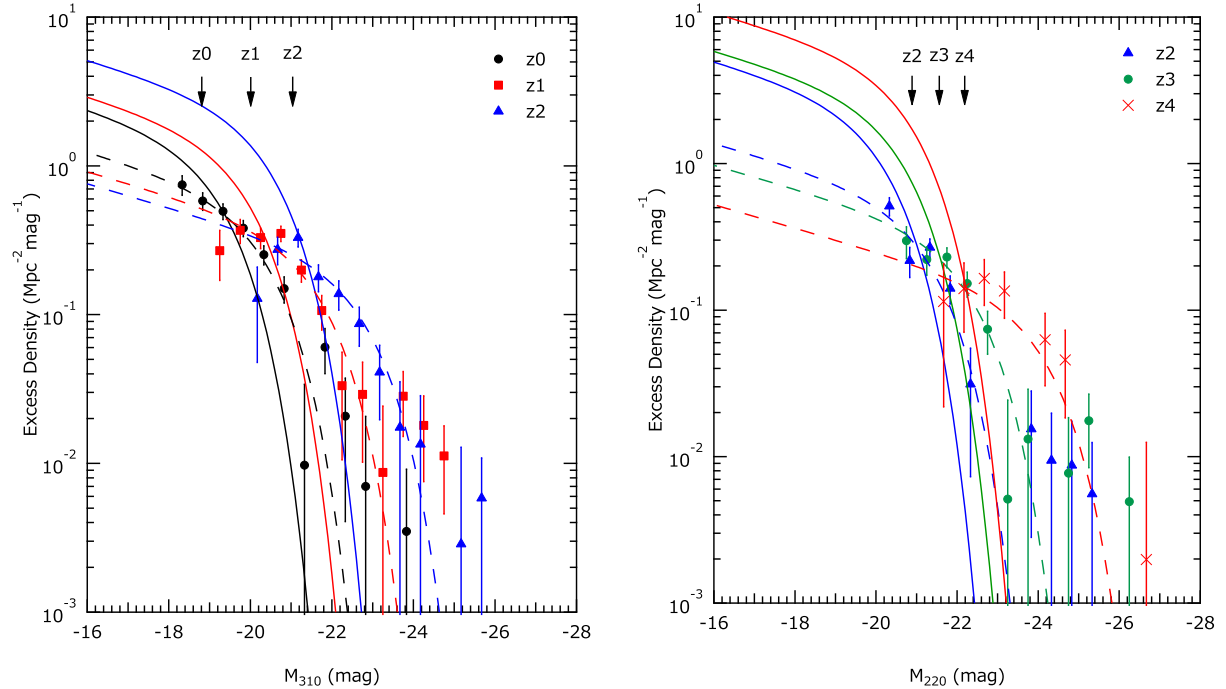


**Fig. 19.** Absolute magnitude distributions of galaxies around AGNs calculated as in equation 17. Detection efficiencies were corrected and plotted for  $M < M_{50}$ . The left panel shows the distributions for z0, z1 and z2 groups. The right panel shows the distributions for z2, z3 and z4 groups. The solid lines represent luminosity function calculated by the parametrization used in this work and scaled by a factor calculated from the cross-correlation length obtained for  $M_{50}$  galaxy samples. The dashed lines represent Schechter functions fitted to the data points. The arrows at the top of the panels indicates the 90% detection limit.

at magnitudes brighter than  $M_*$ , which results in larger clustering of bright galaxies as obtained in section 4.2.

To test if the overdensity can be explained by the uncertainty of  $M_*$  parameter used in the parametrization of luminosity function model (refer to it as  $M_{*,\text{param}}$ ), we measured the  $M_*$  parameters for the observed magnitude distributions (refer to it as  $M_{*,\text{clust}}$ ), by fitted the Schechter function to them. In the fitting  $\alpha$  was fixed to  $-1.2$ . The results are summarized in Table 6 and compared in Figure 20 with the parametrization (thick solid lines) and literature values (open markers). The obtained  $M_{*,\text{clust}}$  parameters are typically smaller (i.e. brighter) than  $M_{*,\text{param}}$  parameter by  $>1$  mag, which well exceeds the uncertainty of  $M_{*,\text{param}}$ ,  $0.28$  mag, expected for the parametrization. Thus it is unlikely that the overdensity is attributed only to the uncertainty of the assumed luminosity function.

To investigate the galaxy type that contributes to the overdensity at the bright end, we derived the magnitude distributions for blue and red galaxy separately. They were classified at  $D_1 = 1.4$  or  $D_2 = 0.8$ . Figure 21 shows the comparisons between the magnitude distributions for blue and red galaxies.  $M_{*,\text{clust}}$  parameters measured for the distributions are summarized in Table 7 and plotted in Figure 22.

**Table 6.** Comparisons of  $M_*$  parameters.

| redshift group | average redshift | wavelength | $M_{*,\text{clust}}^a$ | $M_{*,\text{param}}^b$ | $\Delta M_*^c$ |
|----------------|------------------|------------|------------------------|------------------------|----------------|
|                |                  | nm         | mag                    | mag                    | mag            |
| z0             | 0.81             | 310        | $-20.4 \pm 0.2$        | -19.3                  | 1.1            |
| z1             | 1.26             | 310        | $-21.8 \pm 0.2$        | -20.0                  | 1.8            |
| z2             | 1.75             | 310        | $-22.9 \pm 0.3$        | -20.6                  | 2.3            |
| z2             | 1.76             | 220        | $-21.4 \pm 0.2$        | -20.3                  | 1.1            |
| z3             | 2.26             | 220        | $-22.4 \pm 0.3$        | -20.7                  | 1.7            |
| z4             | 2.74             | 220        | $-24.2 \pm 0.7$        | -21.0                  | 3.2            |

<sup>a</sup>  $M_*$  parameters measured for clustering galaxies around AGN, <sup>b</sup>  $M_*$  parameters calculated from the parametrization as described in section 3.1, <sup>c</sup>  $M_{*,\text{param}} - M_{*,\text{clust}}$ .

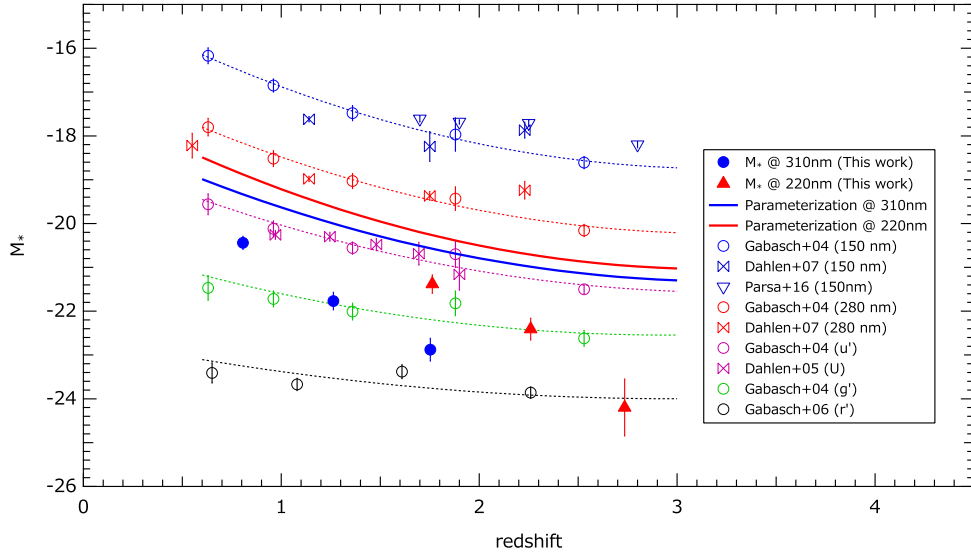


**Fig. 20.** Comparison of  $M_*$  parameters measured for clustering galaxies around AGNs (filled circles and filled triangles) and those calculated from the parametrization (thick solid lines).  $M_*$  values derived in literature (Gabasch et al. 2004, 2006; Dahlen et al. 2005, 2007; Parsa et al. 2016) are also plotted.

The obtained  $M_{*,\text{clust}}$  parameters for red galaxies are systematically brighter than those for blue galaxies by more than two sigma at redshift z0, z1, and z2 for measurements at 310 nm. No statistically significant difference is found for the values for z2, z3, and z4 measured at 220 nm, which is mostly due to poor statistic and lower resolution of  $D_2$  parameter on the deconvolution of the two components.

We also investigated whether there is a difference in the luminosity functions of clustering galaxies for lower and higher BH mass groups. Figure 23 shows the comparisons between the magnitude distributions for M8 and M9 mass groups, and  $M_{*,\text{clust}}$  parameters are summarized in Table 8 and plotted in Figure 24.

The obtained  $M_{*,\text{clust}}$  parameters for M9 group are systematically brighter than those for M8

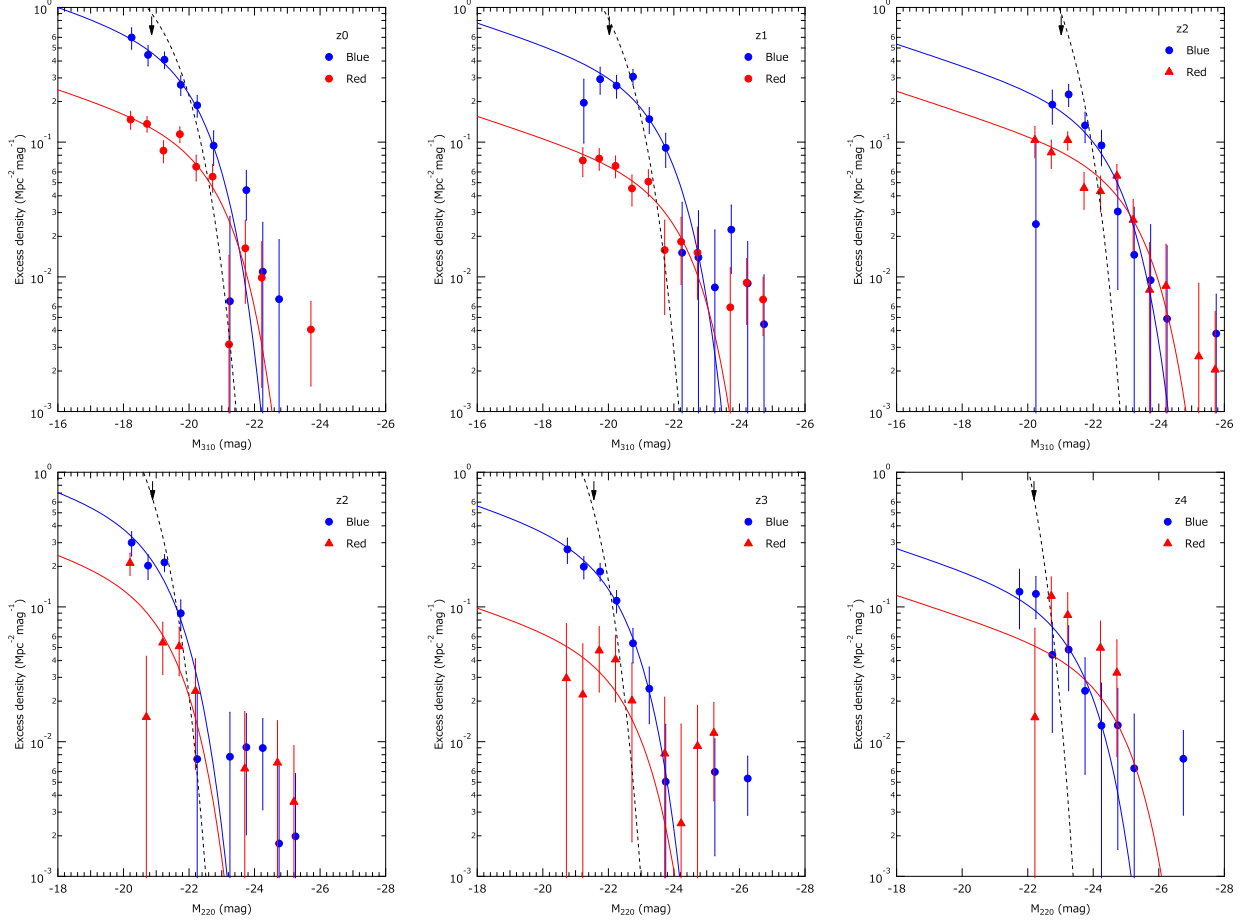


**Fig. 21.** Absolute magnitude distributions for blue and red galaxies. The dashed lines represent luminosity function calculated by the parametrization used in this work and scaled by a factor calculated from the cross-correlation length. The solid lines represent Schechter functions fitted to the data points. The arrows at the top of the panels indicates the 90% detection limit.

group by more than two sigma at redshift  $z_0$  and  $z_1$ . No statistically significant difference is found for the values at redshift  $z_2$  (both for 310 nm and 220 nm) and  $z_3$ . The results may indicate the enhancement of bright galaxies around AGNs with higher BH mass ( $> 10^{8.5} M_{\odot}$ ) at redshift  $< 1.5$ , while at redshift  $\geq 1.5$  the luminosity function of galaxy is similar around AGNs with BH mass of  $\geq 10^8 M_{\odot}$ .

## 5 Discussion and Conclusion

The dependence of AGN-galaxy cross-correlation on redshift, galaxy luminosity, and BH mass was examined. The galaxy samples used in this analysis are dominated with blue type galaxies, and the fractions of blue type galaxies are more than 70%. No significant dependence on the BH mass was found for the cross-correlation length derived by using whole galaxy samples. We, however, obtained indication that cross-correlation with red galaxies is larger for larger BH mass at the lowest

**Table 7.** Comparisons of  $M_*$  parameters measured for clustering galaxies around AGNs for blue and red galaxy types.

| redshift | wavelength | $M_{*,\text{clust}}(\text{blue})$ | $M_{*,\text{clust}}(\text{red})$ |
|----------|------------|-----------------------------------|----------------------------------|
|          |            | mag                               | mag                              |
| z0       | 310        | $-20.29 \pm 0.18$                 | $-20.95 \pm 0.25$                |
| z1       | 310        | $-21.66 \pm 0.23$                 | $-22.29 \pm 0.37$                |
| z2       | 310        | $-22.60 \pm 0.35$                 | $-23.36 \pm 0.36$                |
| z2       | 220        | $-21.28 \pm 0.22$                 | $-21.42 \pm 0.53$                |
| z3       | 220        | $-22.38 \pm 0.20$                 | $-22.67 \pm 1.13$                |
| z4       | 220        | $-23.57 \pm 0.53$                 | $-24.78 \pm 1.43$                |

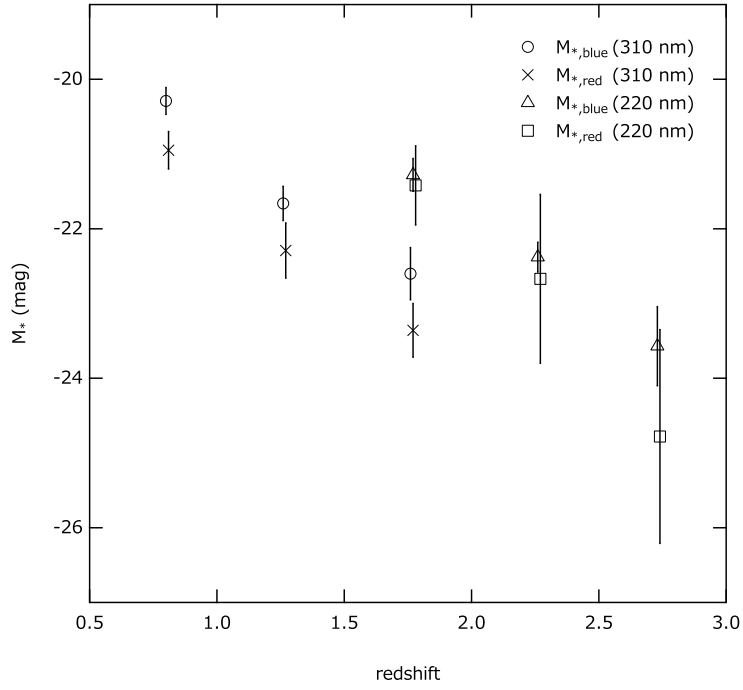


**Fig. 22.** Comparison of  $M_*$  parameters measured for blue and red galaxies.

**Table 8.** Comparisons of  $M_*$  parameters measured for clustering galaxies around AGNs of M8 and M9 groups.

| redshift | wavelength | $M_{*,\text{clust}}(\text{M8})$ | $M_{*,\text{clust}}(\text{M9})$ |
|----------|------------|---------------------------------|---------------------------------|
|          |            | mag                             | mag                             |
| z0       | 310        | $-20.29 \pm 0.24$               | $-20.83 \pm 0.21$               |
| z1       | 310        | $-21.36 \pm 0.40$               | $-22.12 \pm 0.32$               |
| z2       | 310        | $-22.93 \pm 0.34$               | $-23.06 \pm 0.52$               |
| z2       | 220        | $-21.50 \pm 0.32$               | $-21.22 \pm 0.35$               |
| z3       | 220        | $-22.58 \pm 0.41$               | $-22.44 \pm 0.28$               |

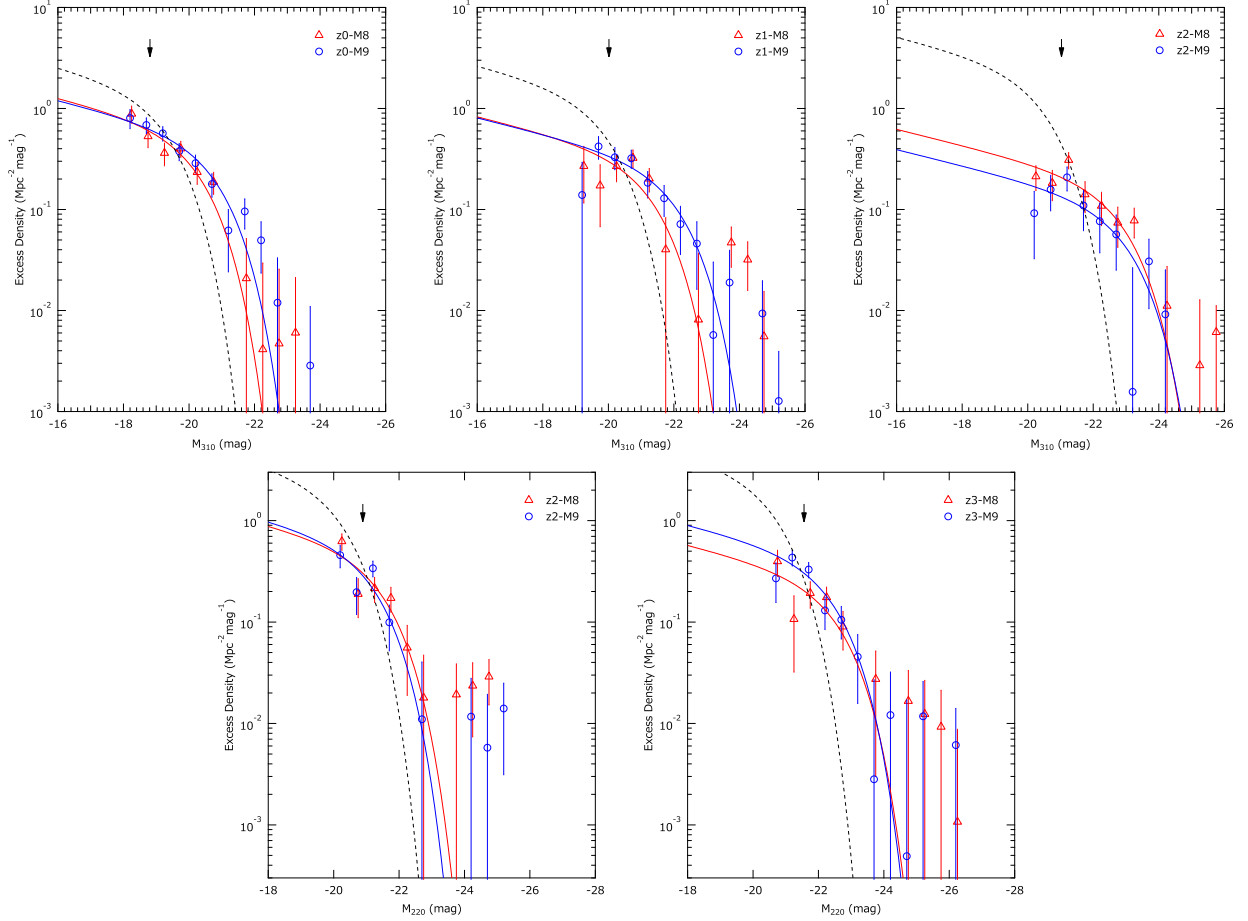


**Fig. 23.** Absolute magnitude distributions for M8 and M9 mass groups. The dashed lines represent luminosity function calculated by the parametrization used in this work and scaled by a factor calculated from the cross-correlation length. The solid lines represent Schechter functions fitted to the data points. The arrows at the top of the panels indicates the 90% detection limit.

redshift group as shown in Figure 12, which is consistent with the previous studies (Komiya et al. 2013; Shirasaki et al. 2016) in which galaxy samples are strongly biased to a red type. These results indicate that the red galaxies around AGNs are related more closely with the evolution of SMBHs in the same system (i.e. dark matter halo) than the blue galaxies are.

The redshift dependence of the cross-correlation length was found as shown in Figure 10, and it turned out to be most primarily due to the luminosity dependence of galaxy clustering and its redshift evolution. The luminosity dependence of galaxy clustering has been reported in literature (e.g. Zehavi et al. 2011; Ishikawa et al. 2015). The observed luminosity dependence can be explained as a result of shift in the  $M_{*,clust}$  parameter by  $>1$  mag to luminous side as shown in section 4.3. This indicates that the starformation activity is relatively larger around AGNs in our sample compared to those in a general field at the same redshift.

We have obtained the luminosity dependence of the cross-correlation length for five redshift

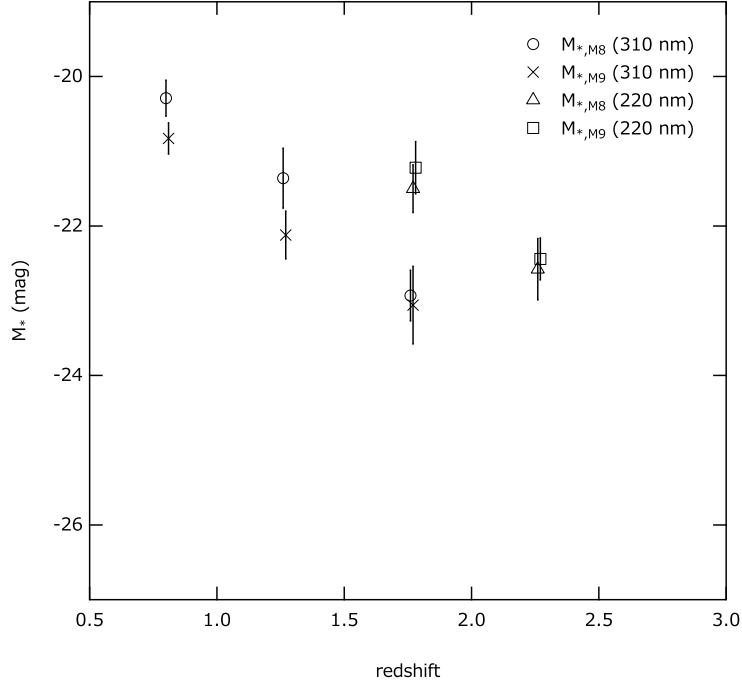


Fig. 24. Comparison of  $M_*$  parameters measured for M8 and M9 groups.

groups separately, and derived an empirical formula to describe the luminosity dependence at redshifts covered by this work and for the galaxy samples used in this analysis. The  $r_{0,min}$  parameter in the formula represents an asymptotic cross-correlation length at lower luminosities and predicts the cross-correlation length between AGNs and ordinary galaxies at that redshift. The obtained values for  $r_{0,min}$  increase from  $7 h^{-1}\text{Mpc}$  at the lowest redshift group ( $z \sim 0.7$ ) to  $10 h^{-1}\text{Mpc}$  at redshifts  $z > 1.5$ , which indicates the increase of auto-correlation length of AGNs and/or galaxy at higher redshifts.

If this increase in the cross-correlation length is attributed only to the increase in auto-correlation of AGNs, the AGN auto-correlation length and power index at  $z > 1.5$  are calculated as  $r_{0,AA} = 25 h^{-1}\text{Mpc}$ ,  $\gamma = -1.9$ , where the cross-correlation of AGNs and galaxies ( $\xi_{AG}$ ) is assumed to be expressed with the auto-correlation of AGNs ( $\xi_{AA}$ ) and galaxies ( $\xi_{GG}$ ) as:

$$\xi_{AG}^2 = \xi_{AA}\xi_{GG}, \quad (22)$$

and the galaxy auto-correlation is assumed to be unchanged from the value measured by Zehavi et al. (2011) at redshift  $< 0.25$ , that is  $r_{0,GG} = 3.6 h^{-1}\text{Mpc}$  and  $\gamma = -1.7$ . The estimate for the assumption is significantly larger than that obtained by Ross et al. (2009), who reported  $13.51 \pm 1.81 h^{-1}\text{Mpc}$  for  $\gamma = 2.0$  at redshift  $> 2$ , even after corrected for the difference in  $\gamma$ . So the increase in the auto-correlation of galaxies is required to reproduce the cross-correlation length measured at  $z > 2.0$ .

The fraction of red galaxies in the environment can be a measure of the degree of progress on

galaxy formation and evolution in that system. The fraction may depend on the frequency of events that trigger the starformation activity, such as major/minor merger and/or interaction with a nearby galaxy, and also the time scale of the starformation quenching. If the frequency of the triggering event is higher and the time scale of the quenching is shorter, the galaxy formation and evolution rapidly proceed and the red galaxy fraction is increased in such an environment. In such an environment, it is also expected that the SMBHs rapidly increase their mass through the mass accretion caused by a similar kind of event which triggers the starformation in the galaxies around it.

As blue galaxies are dominated, the transformation of only a small fraction of blue galaxies to red galaxies can significantly affect to the clustering strength of the red galaxies. This can be the explanation for that the clustering of whole galaxies (both blue and red galaxies) are almost independent of the BH mass, while the clustering of red galaxies depend on the BH mass as reported in (Komiya et al. 2013; Shirasaki et al. 2016).

It was measured that the peak position of the color distributions for blue galaxies shifts to redder side as the increase of redshift. This is, at least partly, due to the the luminosity dependence of the peak position. This result may indicate that the luminous starforming galaxies at these redshifts are reddened by dust or by some other mechanism.

We demonstrated that HSC-SSP imaging data alone can be a powerful tool to investigate the environment of AGNs at intermediate redshifts up to 3.0. The current S15b dataset covers 250 deg<sup>2</sup> of sky which is only 1/5 of the planned survey area. By using the final dataset, we can significantly improve the measurement on the characteristics of environmental galaxies around AGNs, their dependence on types of AGN, and also their redshift evolution. It is also important to combine dataset taken at other wavelengths especially infrared bands, which improves the selection of galaxies that are located at the AGN redshift and also the distinction of red and blue type galaxies at higher redshifts, and enable to measure the properties of dust obscured populations which are not detected in the HSC. The analysis method utilized in this work can be adapted to other type of extragalactic objects with known redshift.

In this work we focused on the AGNs which have BHs with relatively larger mass of  $M_{\text{BH}} \geq 10^7 M_{\odot}$ . It is also required to investigate the AGNs with lower BH mass and compare the difference on their environment to understand their effect on the evolution of SMBH. Those AGNs will be identified by the follow up observations of the candidate AGNs discovered in the HSC-SSP dataset. The future Subaru Prime Focus Spectrograph (PFS) survey project will also provide dataset of those AGNs, and it will provide an essential dataset to directly measure the environment of individual AGN.

## Acknowledgments

The authors would like to thank Michael Strauss for valuable comments. The Hyper Suprime-Cam (HSC) collaboration includes the astronomical communities of Japan and Taiwan, and Princeton University. The HSC instrumentation and software were developed by the National Astronomical Observatory of Japan (NAOJ), the Kavli Institute for the Physics and Mathematics of the Universe (Kavli IPMU), the University of Tokyo, the High Energy Accelerator Research Organization (KEK), the Academia Sinica Institute for Astronomy and Astrophysics in Taiwan (ASIAA), and Princeton University. Funding was contributed by the FIRST program from Japanese Cabinet Office, the Ministry of Education, Culture, Sports, Science and Technology (MEXT), the Japan Society for the Promotion of Science (JSPS), Japan Science and Technology Agency (JST), the Toray Science Foundation, NAOJ, Kavli IPMU, KEK, ASIAA, and Princeton University. This paper makes use of software developed for the Large Synoptic Survey Telescope. We thank the LSST Project for making their code available as free software at <http://dm.lsst.org>. Funding for the Sloan Digital Sky Survey IV has been provided by the Alfred P. Sloan Foundation, the U.S. Department of Energy Office of Science, and the Participating Institutions. SDSS-IV acknowledges support and resources from the Center for High-Performance Computing at the University of Utah. The SDSS web site is [www.sdss.org](http://www.sdss.org). The Pan-STARRS1 Surveys (PS1) have been made possible through contributions of the Institute for Astronomy, the University of Hawaii, the Pan-STARRS Project Office, the Max-Planck Society and its participating institutes, the Max Planck Institute for Astronomy, Heidelberg and the Max Planck Institute for Extraterrestrial Physics, Garching, The Johns Hopkins University, Durham University, the University of Edinburgh, Queen's University Belfast, the Harvard-Smithsonian Center for Astrophysics, the Las Cumbres Observatory Global Telescope Network Incorporated, the National Central University of Taiwan, the Space Telescope Science Institute, the National Aeronautics and Space Administration under Grant No. NNX08AR22G issued through the Planetary Science Division of the NASA Science Mission Directorate, the National Science Foundation under Grant No. AST-1238877, the University of Maryland, and Eotvos Lorand University (ELTE) SDSS-IV is managed by the Astrophysical Research Consortium for the Participating Institutions of the SDSS Collaboration including the Brazilian Participation Group, the Carnegie Institution for Science, Carnegie Mellon University, the Chilean Participation Group, the French Participation Group, Harvard-Smithsonian Center for Astrophysics, Instituto de Astrofísica de Canarias, The Johns Hopkins University, Kavli Institute for the Physics and Mathematics of the Universe (IPMU) / University of Tokyo, Lawrence Berkeley National Laboratory, Leibniz Institut für Astrophysik Potsdam (AIP), Max-Planck-Institut für Astronomie (MPIA Heidelberg), Max-Planck-Institut für Astrophysik (MPA Garching), Max-Planck-Institut für Extraterrestrische Physik (MPE), National Astronomical Observatories of China, New Mexico State University, New York University, University of Notre Dame, Observatório Nacional / MCTI, The Ohio State University, Pennsylvania State University, Shanghai Astronomical Observatory, United Kingdom Participation Group, Universidad Nacional Autónoma de México, University of Arizona, University of Colorado Boulder, University of Oxford, University of Portsmouth, University of Utah, University of Virginia, University of Washington, University of Wisconsin, Vanderbilt University, and Yale University.

## References

- Aihara, H., et al. 2017, PASJ, in prep
- Aihara, H., et al. 2017, PASJ, in prep
- Allevato, V., et al. 2011, ApJ, 736, 99
- Axelrod, T.; Kantor, J.; Lupton, R. H.; Pierfederici, F. 2010, Proceedings of the SPIE, 7740, 774015.
- Bradshaw, E. J., et al. 2011, MNRAS, 415, 2626
- Brammer, G. B., van Dokkum, P. G., Coppi, P. 2008, ApJ, 686, 1503
- Ciotti, L., Ostriker, J. P. 2001, ApJ, 551, 131
- Ciotti, L., Ostriker, J. P. 2007, ApJ, 665, 1038

Coatman, L., et al. 2016, MNRAS, 465, 2120  
Coil, A. L., et al. 2009, ApJ, 701, 1484  
Croom, S. M., et al. 2005, MNRAS, 356, 415  
Dahlen, T., et al. 2005, ApJ, 631, 126  
Dahlen, T., et al. 2007, ApJ, 654, 172  
Donoso, E., Li, Cheng, Kauffmann, G., Best, P. N. and Heckman, T. M. 2010, MNRAS, 407, 1078  
Fanidakis, N. et al., 2013, MNRAS, 436, 315  
Ferrarese, L., Merritt, D. 2000, ApJ, 539, L9  
Gabasch, A. et al. 2004, A&A, 421, 41  
Gabasch, A. et al. 2006, A&A, 448, 101  
Gebhardt, K., et al. 2000, ApJ, 539, L13  
Georgakakis, A., et al. 2014, MNRAS, 443, 3327  
Hickox, R. C., et al., 2009, ApJ, 696, 891  
Ho, L. C. 2007, ApJ, 668, 94  
Hopkins, P. F., Hernquist, L., Cox, T. J., Keres, D. 2008, ApJS, 175, 356  
Ikeda, H., et al. 2015, ApJ, 809, 138  
Ishikawa, S., et al. 2015, MNRAS, 454, 205  
Ivezic, Z., et al. 2008, arXiv:0805.2366  
Keres, D., et al., 2009, MNRAS, 395, 160  
Komiya, Y., Shirasaki, Y., Ohishi, M., Mizumoto, Y., 2013, ApJ, 775, 43  
Kormendy, J. & Ho, Kennicutt, R. C., Jr. 2004, ARA&A, 42, 603  
Kormendy, J. & Ho, L. C. 2013, ARA&A, 51, 511  
Krolewski, A., G., Eisenstein, D. J. 2015, ApJ, 803, 4  
Krumpe, M., Miyaji, T., Coil, A. L., and Aceves, H. 2012, ApJ, 746, 1  
Krumpe, M., et al. 2015, ApJ, 815, 21  
Magnier, E. A., et al. 2013, ApJS, 205, 20  
Magorrian, J., et al. 1998, AJ, 115, 2285  
Mejia-Restrepo, J. E. et al., 2016, MNRAS, 460, 187  
Menci, M., Gatti, M., Fiore, F., & Lamastra, A. 2014, A&A, 569, A37  
Miyazaki, S. et al., 2012, Proc. SPIE 8446, 0Z  
Miyazaki, S. et al., 2017, PASJ, in prep.  
Mountrichas, G., et al. 2013, MNRAS, 430, 661  
Paris, I. et al. 2017, A&A, 597, A79  
Parsa, S. et al. 2016, MNRAS, 456, 3194

Richstone, D., et al. 1998, *Nature*, 395, A14  
Ross, N. P., et al. 2009, *ApJ*, 697, 1634  
Sanders, D. B., et al. 1988, *ApJ*, 325, 74  
Schlafly, E. F., et al. 2012, *ApJ*, 756, 158  
Schlegel, D. J., Finkbeiner, D. P., & Davis M. 1998, *ApJ*, 500, 525  
Shen, Y. et al., 2011, *ApJS*, 194, 45  
Shirasaki, Y., et al. 2011, *PASJ*, 63, 469  
Shirasaki, Y., et al. 2016, *PASJ*, 68, 23  
Silverman, J. D., et al. 2009, *ApJ*, 695, 171  
Tonry, J. L., et al. 2012, *ApJ*, 750, 99  
Treister, E., Schawinski, K, Urry, C. M., & Simmons, B. D. 2012, *ApJ*, 758, L39  
Zehavi, I., et al. 2011, *ApJ*, 736, 59  
Zhang, S., Wang, T., Wang, H., Hongyan, Z. 2013, *ApJ*, 773, 175